


Commensuration effects on skyrmion Hall angle and drag for manipulation of skyrmions on two-dimensional periodic substrates

C. Reichhardt and C. J. O. Reichhardt *Theoretical Division and Center for Nonlinear Studies, Los Alamos National Laboratory, Los Alamos, New Mexico 87545, USA*

(Received 1 February 2022; revised 17 June 2022; accepted 22 June 2022; published 29 June 2022)

We examine the dynamics of an individually driven skyrmion moving through a background lattice of skyrmions coupled to a 2D periodic substrate as we vary the ratio of the number of skyrmions to the number of pinning sites across commensurate and incommensurate conditions. As the skyrmion density increases, the skyrmion Hall angle is nonmonotonic, dropping to low or zero values in commensurate states and rising to an enhanced value in incommensurate states. Under commensuration, the driven skyrmion is channeled by a symmetry direction of the pinning array and exhibits an increased velocity. At fillings for which the skyrmion Hall angle is zero, the velocity has a narrow band noise signature, while for incommensurate fillings, the skyrmion motion is disordered and the velocity noise is broad band. Under commensurate conditions, multi-step depinning transitions appear and the skyrmion Hall angle is zero at low drives but becomes finite at higher drives, while at incommensurate fillings there is only a single depinning transition. As the gyrotropic component of the skyrmion dynamics, called the Magnus force, increases, peaks in the velocity that appear in commensurate regimes cross over to dips, and new types of directional locking effects can arise in which the skyrmion travels along other symmetry directions of the background lattice. At large Magnus forces, and particularly at commensurate fillings, the driven skyrmion can experience a velocity boost in which the skyrmion moves faster than the applied drive due to the alignment of the Magnus-induced velocity with the driving direction. In some cases, an increase of the Magnus force can produce regimes of enhanced pinning when the skyrmion is forced to move along a nonsymmetry direction of the periodic pinning array. This is in contrast to systems with random pinning, where increasing the Magnus force generally reduces the pinning effect. We demonstrate these dynamics for both square and triangular substrates and map out the different regimes as a function of filling fraction, pinning force, and the strength of the Magnus force in a series of dynamic phase diagrams.

DOI: [10.1103/PhysRevB.105.214437](https://doi.org/10.1103/PhysRevB.105.214437)

I. INTRODUCTION

Magnetic skyrmions are particle-like spin textures found in numerous systems [1–8], including materials in which the skyrmions are stable at room temperature [9–12]. Skyrmions can also be generated by an applied current [13–20]. Due to their size scale, mobility, and stability, skyrmions are promising candidates for a variety of applications [21–24], many of which require the ability to control how the skyrmions move, how they interact with defects or nanostructures, and how to manipulate them on the individual level. The skyrmions also interact with quenched disorder in the system, giving rise to a pinning effect and establishing a threshold driving force that must be applied for the skyrmion to be set in motion [25–31]. The magnitude of this threshold depends on the properties of the disorder [25,32–34], collective interactions with other skyrmions [35], and thermal effects [36–38]. There are also other types of skyrmions and skyrmionlike textures [39], including ferromagnetic [1,2] and antiferromagnetic [40,41] skyrmions, antiskyrmions [42,43], and merons [44].

For ferromagnetic skyrmions subjected to an applied drive, the skyrmion motion exhibits a skyrmion Hall effect along the skyrmion Hall angle [3,45,46] θ_{sk} , which arises from the topology of the skyrmions. The intrinsic skyrmion Hall angle $\theta_{\text{sk}}^{\text{int}}$ is proportional to the ratio of the Magnus or

gyrotropic term to the dissipative term of the skyrmion dynamics. Many proposed skyrmion applications require the reduction or absence of the skyrmion Hall effect, so there have been numerous studies focused on understanding how to control the skyrmion Hall angle, such as by the use of nanostructures [25,31]. The magnitude of the skyrmion Hall effect is modified both by the pinning landscape and by the velocity of the skyrmions. Quenched disorder induces a side jump effect that reduces the skyrmion Hall angle below its intrinsic value. The side jump is largest for small velocities just above depinning, giving a skyrmion Hall angle that is zero at depinning and increases with increasing drive until it saturates at a value near $\theta_{\text{sk}}^{\text{int}}$ for high drives [19,30,38,47–55]. The skyrmion Hall angle can also be affected by shape distortions of the skyrmions and collisions with other skyrmions [30,38,56,57]. In addition to the importance of understanding skyrmion dynamics in the presence of disorder for applications, the strong gyrotropic nature of the dynamics means that skyrmions represent a new class of systems that can show collective dynamics when driven over random or periodic substrates. Most previous studies of such behavior have involved overdamped systems [25].

One approach to generating well-controlled skyrmion motion is to couple the skyrmions to nanostructures, such as

a periodic array of defects or other types of engineered landscapes [21,22,25,58–61]. In this case, it is important to understand how individual skyrmions interact with both the defect array and with the other skyrmions. An example of such a system is skyrmions interacting with a two-dimensional (2D) periodic substrate, where the system can be characterized by a filling factor f corresponding to the ratio of the number of skyrmions N_s to the number of pinning sites N_p . When $f = N_s/N_p$ is an integer, the skyrmions form a commensurate or ordered crystalline structure. Commensuration effects for particles on 2D substrates have been studied extensively in other condensed matter systems, such as the ordering of atoms or molecules on surfaces [62], sliding friction [63], colloidal particles on patterned substrates [64,65], dusty plasmas [66], Wigner crystal ordering in moiré systems [67], vortices in Bose Einstein condensates [68], and cold atoms coupled to optical traps [69]. The closest match to the skyrmion system, however, is vortices in type-II superconductors coupled to 2D pinning arrays [70–75]. At commensuration, the superconducting vortices form an ordered lattice and exhibit a strong enhancement of the pinning effect observable as peaks in the depinning threshold as a function of changing superconducting vortex density.

Commensurate-incommensurate systems display a rich variety of dynamical phases since the collective motion differs at commensurate and incommensurate fillings [25]. For example, there can be multiple step depinning, transitions between ordered and disordered flow [76,77], and soliton motion [78]. Particle flow on 2D periodic substrates can be modified significantly depending on the direction of drive with respect to symmetry directions of the underlying substrate. For example, in directional or symmetry locking, the particles preferentially move along certain symmetry directions of the pinning lattice even when the drive is not aligned with those directions, and as a result, for changing drive orientation a series of steps appear in the velocity versus driving angle curves [79–84]. Since the skyrmion Hall angle depends on the magnitude of the drive in systems with pinning, when individual skyrmions move over 2D periodic substrates, numerical studies have shown that the skyrmion motion locks to different substrate symmetry directions as the magnitude of the drive increases [48,85,86]. For a square array, such locking directions include 0° and 45° from a primary lattice vector. In general, locking of skyrmions moving on a square array can occur at angles $\phi = \arctan(n/m)$ from the primary symmetry axis, with integer n and m ; however, the size of the pinning sites as well as interactions with other skyrmions can limit which symmetry directions are accessible. Other studies for skyrmions on 2D pinning arrays indicate that different types of crystalline ordering occur at the matching fields [87] and that large scale collective flow states can arise under bulk driving [88]. In micromagnetic simulations, skyrmions moving on a 2D pinning array exhibit a number of different dynamic phases that could be useful for applications [89]. In addition, there are now various experiments on skyrmion states in periodic one-dimensional (1D) [61] and 2D pinning arrays [90].

In this work, we examine the dynamics of skyrmions on a 2D square or triangular pinning lattice. We drive a single skyrmion that interacts both with the other skyrmions and directly with the substrate, and measure the velocity and di-

rection of motion of the driven skyrmion as the system passes through a series of commensurate-incommensurate transitions at varied pinning strength and varied ratios of the Magnus term to the dissipative term. This work builds upon our previous studies examining the dynamics of individually driven superconducting vortices [91,92] and skyrmions [93,94] interacting with either a background lattice of particles or with pinning. In the case of superconducting vortices where the motion is overdamped, numerous methods to drive individual vortices, including nanotips [95,96] and optical trapping [97,98], have been studied in experiments and simulations. Individual skyrmions can also be driven with different types of tips [99], local magnetic field gradients [100,101], and with optical trapping [102–104]. The method of driving individual particles through a background of other particles while measuring the drag on the driven particle from fluctuations is known as active rheology and has been studied experimentally and theoretically for colloidal particles [105–109], granular matter [110–112], active matter [113], and superconducting vortex systems [91,96,114,115].

In most active rheology studies, under a constant driving force the velocity of the driven particle decreases as the density of the system increases due to an increase in the frequency of collisions with background particles, and there can be a sudden drop to zero motion or a pinning transition when the system passes through a critical density into a glass, jammed, crystalline, or amorphous solid state. In our previous work on active rheology in a skyrmion system, we considered a single skyrmion driven through a background of other skyrmions in the absence of pinning [93]. For a constant driving force, we found that the skyrmion Hall angle decreases with increasing skyrmion density due to enhanced collisions; however, particularly for systems with a strong Magnus force, we also found a counter-intuitive increase in the velocity, or a boost effect, in which the skyrmion velocity increases with increasing system density. In some cases, the skyrmion velocity is larger than what it would be in the absence of collisions with other skyrmions. This boost effect arises from a combination of the skyrmion Hall effect and density fluctuations created in the surrounding skyrmions by the driven skyrmion. The density gradient forms perpendicular to the direction of the drive and exerts a repelling force on the driven particle along this direction, but the Magnus term generates a velocity perpendicular to this repelling force and parallel to the drive. This is example of what is known as an odd-viscosity effect of the type observed in chiral systems with gyroscopic forces [116–119]. We have also considered single driven skyrmions interacting with other skyrmions in the presence of random quenched disorder, where in addition to velocity boost phenomena, we observe several pinned and jammed phases as well as stick-slip motion [94].

For overdamped systems, we have also numerically examined the active rheology of superconducting vortices and colloidal particles interacting with 2D periodic pinning arrays as the filling factor of the system is varied. Here we observe what we call an anti-commensuration effect in which the drag on the driven particle is reduced at commensurate matching conditions [92], opposite from the behavior found in bulk driven systems [70,72–75]. The drag reduction at commensuration appears when the surrounding particles

become strongly coupled to the substrate at matching conditions and cannot be dragged along by the driven particle, whereas at incommensurate fillings, the surrounding particles are much more weakly coupled to the substrate, permitting the driven particle to drag background particles and increasing the effective viscosity it experiences. The result is a strongly non-monotonic drag that shows a series of peaks at the matching conditions. In the case of an individual skyrmion driven over a 2D periodic array at commensurate and incommensurate conditions, the Magnus force produces much more complex dynamics than are found in the overdamped superconducting vortex system [92].

In this work, we demonstrate that active rheology for a skyrmion driven through a background lattice in the presence of a 2D periodic pinning array produces very different behavior from that found for random pinning [94] or in the absence of pinning [93]. The skyrmion Hall angle is non-monotonic, falling to zero at commensurate conditions where the skyrmions form an ordered lattice and the skyrmion velocity peaks. For strong Magnus forces, the skyrmion Hall angle remains finite but is still reduced at the matching conditions. In general, the skyrmion motion is ordered at commensurate conditions and disordered at incommensurate fillings. For increasing Magnus force, there are more extended regions of finite drive for which the skyrmion remains pinned, a behavior that is the opposite of what is found for bulk driven systems with random pinning. At strong Magnus forces, under commensurate conditions we observe a pronounced velocity boost effect where the driven skyrmion moves faster than it would if there were no substrate and no collisions with other skyrmions. This boost occurs when the direction of motion of the driven skyrmion becomes locked along an interstitial channel and the driven skyrmion experiences a perpendicular repulsion from the skyrmions trapped in the pinning sites, which is converted by the Magnus term to a velocity in the direction of drive. This effect is similar to the velocity enhancement found for skyrmions moving along sample edges [120,121]. For higher Magnus forces, the motion becomes increasingly chaotic and the effect of the substrate is strongly reduced.

We mainly focus on the dynamics of a single driven skyrmion; however, we also propose some alternative geometries involving bulk driving near the first matching field where most of the skyrmions are trapped at pinning sites and a small number of skyrmions are in the interstitial regions. For a window of applied drives, the skyrmions in the pinning sites remain pinned but the interstitial skyrmions move and experience interactions with the pinned skyrmions. We have also investigated the effect of finite temperature and find that under commensurate conditions, the behavior changes only when the temperature becomes so high that thermally activated hopping of skyrmions out of the pinning sites begins to occur. Our system could be realized using skyrmions in an array of nanostructured pinning sites created optically, via irradiation, or with lithography. Ideally the system should have low intrinsic pinning so that the driven skyrmion will only interact with the other skyrmions or with the added pinning sites. Recent experiments have demonstrated how to create well defined trapping and guiding sites with irradiation [122]. It would also be possible to use an array of disk shaped defects [123].

II. SIMULATION AND SYSTEM

We consider a 2D system of size $L \times L$ with periodic boundary conditions in the x and y directions containing a square pinning array with lattice constant a . The total number of pinning sites is N_p , giving a pinning density of $n_p = N_p/L^2$. The sample contains N_s interacting skyrmions that are modeled as point particles according to a modified Thiele equation [36,49], in which the skyrmions have repulsive interactions with each other and attractive interactions with the pinning sites. We characterize the system by a filling factor $f = N_s/N_p$. For integer values of f , the system is commensurate and adopts a defect-free crystalline ordering, while for incommensurate fillings, the system either becomes amorphous or forms a crystalline state containing interstitials or vacancies [25]. For certain fractional fillings, such as $f = 1/2$ or $f = 3/2$, the system can be partially ordered [124,125]. Each pinning site has a finite spatial extent, so individual skyrmions can sit either inside a pinning site or in the interstitial regions between the pinning sites depending on the filling factor and the pinning strength. From previous studies of superconducting vortices interacting with 2D square periodic pinning arrays, it is known that the particles will form a square lattice with all of the pinning sites occupied for $f = 1.0$, a checkerboard pattern with half of the particles in interstitial sites at $f = 2.0$, an ordered lattice of dimers at $f = 3.0$, and a hexagonal lattice at $f = 4.0$ [71,73,74,126]. The initial skyrmion positions are obtained by performing simulated annealing from a high temperature molten state down to $T = 0$, as in previous work [73]. After the system is initialized, we insert an additional interstitial skyrmion that is coupled to an applied driving force. This driven particle interacts both with the pinning sites and with the other skyrmions.

The equation of motion for skyrmion i is given by

$$\alpha_d \mathbf{v}_i + \alpha_m \hat{\mathbf{z}} \times \mathbf{v}_i = \mathbf{F}_i^{\text{ss}} + \mathbf{F}_i^p + \mathbf{F}_i^D, \quad (1)$$

where the skyrmion velocity is $\mathbf{v}_i = d\mathbf{r}_i/dt$. The first term on the left with damping constant α_d is the dissipation that aligns the skyrmion motion in the direction of the net applied force. The second term on the left is the Magnus force of magnitude α_m that generates a velocity component perpendicular to the net force. The skyrmion-skyrmion interaction is described by $\mathbf{F}_i^{\text{ss}} = \sum_{j=1}^{N_s} K_1(r_{ij}) \hat{\mathbf{r}}_{ij}$, where the distance between skyrmion i and skyrmion j is $r_{ij} = |\mathbf{r}_i - \mathbf{r}_j|$, $\hat{\mathbf{r}}_{ij} = (\mathbf{r}_i - \mathbf{r}_j)/r_{ij}$, and K_1 is the modified Bessel function which decays exponentially for large r [36]. The pinning sites are modeled as finite-range parabolic potential traps of radius r_p that exert a maximum pinning force of F_p , giving $\mathbf{F}_i^p = \sum_{k=1}^{N_p} (F_p/r_p)(\mathbf{r}_i - \mathbf{r}_k^{(p)}) \Theta(r_p - |\mathbf{r}_i - \mathbf{r}_k^{(p)}|) \hat{\mathbf{r}}_{ik}^{(p)}$, where Θ is the Heaviside step function. We fix the pinning density to $n_p = N_p/L^2 = 0.4882$ throughout this work.

The driving force is $\mathbf{F}^D = F_D \hat{\mathbf{x}}$ for the driven skyrmion and $\mathbf{F}^D = 0$ for all of the other background skyrmions, and the driving is always applied along the positive x direction. In the absence of other skyrmions or pinning, the driven skyrmion will move with an intrinsic skyrmion Hall angle of $\theta_{\text{sk}}^{\text{int}} = \arctan(\alpha_m/\alpha_d)$. Pinning and skyrmion-skyrmion collisions can modify the observed skyrmion Hall angle, $\theta_{\text{sk}} = \arctan(\langle V_y \rangle / \langle V_x \rangle)$, where $\langle V_x \rangle$ is the average velocity along the driving direction and $\langle V_y \rangle$ is the average velocity

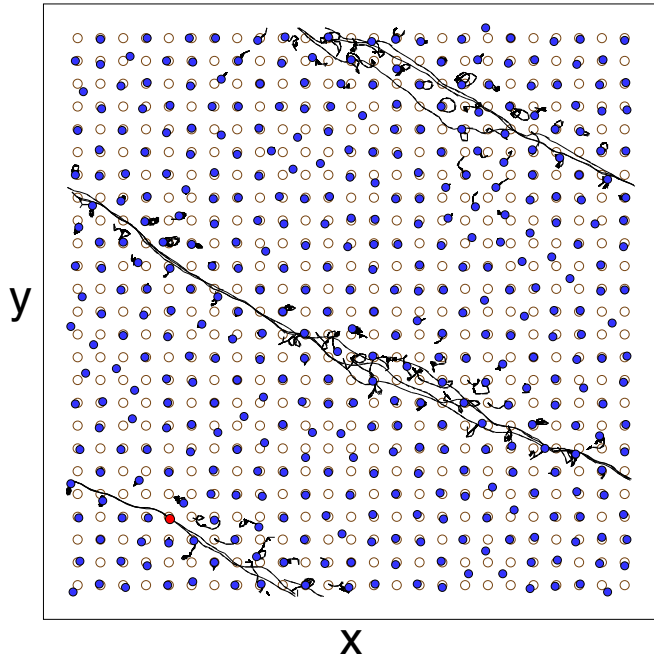


FIG. 1. Image of a sample containing a square pinning lattice showing background skyrmions (blue filled circles), pinning site locations (brown circles), the driven skyrmion (red filled circle), and the skyrmion trajectories (black lines) during a fixed time window. Here, $F_p = 0.25$, $\alpha_m/\alpha_d = 1.0$, $\theta_{\text{sk}}^{\text{int}} = -45^\circ$, and $F_D = 1.0$ at an incommensurate filling of $f = 0.62$ where the background skyrmions are disordered. The driven skyrmion moves in a disordered manner along $\theta_{\text{sk}} = -27^\circ$.

perpendicular to the drive. For convenience, we use the normalization condition $(\alpha_d^2 + \alpha_m^2)^{1/2} = 1.0$. This constraint ensures that we always have $\langle V \rangle = ((V_x)^2 + (V_y)^2)^{1/2} = 1.0$ for $F_D = 1.0$ in the absence of pinning regardless of the value of $\theta_{\text{sk}}^{\text{int}}$. It also makes a velocity boost easy to detect, since for example if $F_D = 1.0$, there is a boost whenever $\langle V \rangle > 1.0$. We increment F_D from zero to a maximum value, spending 2×10^6 to 5×10^6 simulation time steps at each driving force increment in order to obtain a stationary state average velocity measurement.

III. SKYRMION HALL ANGLE AT COMMENSURATE AND INCOMMENSURATE FILLINGS

In Fig. 1, we show a snapshot of a system containing a square pinning lattice with $F_p = 0.25$, $\alpha_m/\alpha_d = 1.0$, $\theta_{\text{sk}}^{\text{int}} = -45^\circ$, and $F_D = 1.0$ at an incommensurate filling of $f = 0.62$ where the background skyrmions are disordered. The skyrmion follows a disordered trajectory with $\theta_{\text{sk}} = -27^\circ$, indicating that the interactions with the pinning and the other skyrmions have depressed the magnitude of θ_{sk} below that of its intrinsic value $\theta_{\text{sk}}^{\text{int}}$.

In Fig. 2(a), we plot $\langle V_x \rangle$ and $\langle V_y \rangle$ versus filling fraction f for the system in Fig. 1. Figure 2(b) shows the net skyrmion velocity $\langle V \rangle$ and Fig. 2(c) illustrates the corresponding $\theta_{\text{sk}} = \arctan(\langle V_y \rangle / \langle V_x \rangle)$. In the limit $f = 0$ where only the driven skyrmion is present, $\langle V \rangle = 1.0$ and $\theta_{\text{sk}} = 45^\circ$. As f increases, $\langle V_y \rangle$ and θ_{sk} both go to zero at $f = 1.0$, where a peak appears

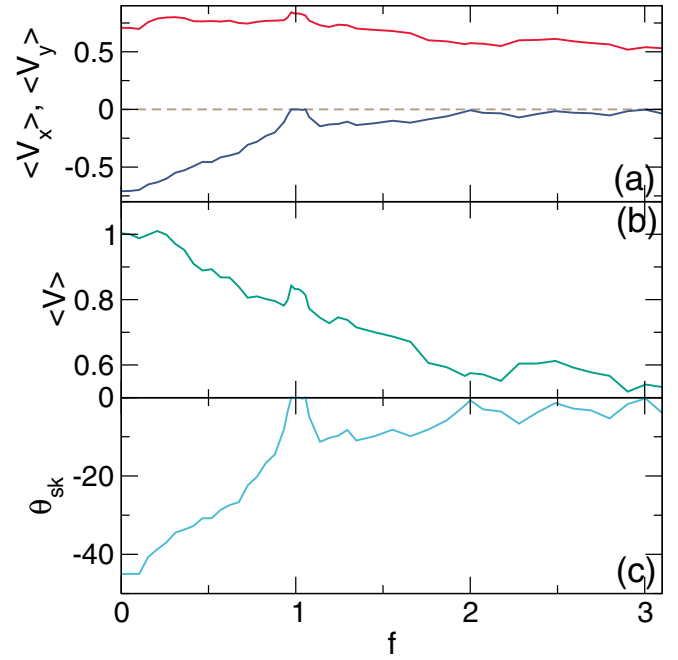


FIG. 2. Behavior under varied filling fraction $f = N_s/N_p$ for the system shown in Fig. 1 with a square pinning array, $F_p = 0.25$, $\alpha_m/\alpha_d = 1.0$, $\theta_{\text{sk}}^{\text{int}} = -45^\circ$, and $F_D = 1.0$. (a) $\langle V_x \rangle$ (red) and $\langle V_y \rangle$ (blue) vs f . (b) $\langle V \rangle = ((V_x)^2 + (V_y)^2)^{1/2}$ vs f . (c) $\theta_{\text{sk}} = \arctan(\langle V_y \rangle / \langle V_x \rangle)$ vs f , which goes to zero at commensurate fillings $f = 1.0$ and $f = 2.0$.

in both $\langle V_x \rangle$ and $\langle V \rangle$. In Fig. 3(a), we show a blow up of the skyrmion motion at $f = 1.0$ for the system in Fig. 2. The background skyrmions form an ordered commensurate square lattice, while the driven skyrmion moves along a 1D interstitial channel between two adjacent pinning rows. As f is further increased, $\langle V_y \rangle$ and θ_{sk} become finite again over the range $1.0 < f < 2.0$ and the skyrmion Hall angle becomes finite, as illustrated in Fig. 3(b) at $f = 1.14$ where $\theta_{\text{sk}} = -10^\circ$. The magnitude of the skyrmion Hall angle is smaller than that

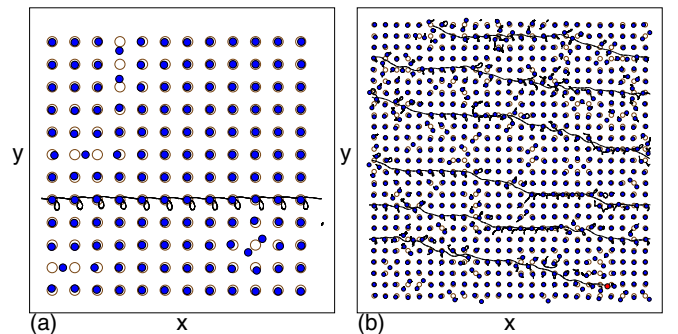


FIG. 3. Images of samples containing a square pinning lattice showing background skyrmions (blue filled circles), pinning site locations (brown circles), the driven skyrmion (red filled circle), and the skyrmion trajectories during a fixed time window for the system from Fig. 1 with $F_p = 0.25$, $\alpha_m/\alpha_d = 1.0$, $\theta_{\text{sk}}^{\text{int}} = -45^\circ$, and $F_D = 1.0$. (a) A portion of the sample at $f = 1.0$, where $\theta_{\text{sk}} = 0^\circ$. Here the driven skyrmion is outside of the visible frame. (b) The entire sample at $f = 1.14$, where $\theta_{\text{sk}} = -10^\circ$.

of $\theta_{\text{sk}}^{\text{int}}$ due to the larger number of skyrmion-skyrmion collisions that occur at the higher densities. At $f = 2.0$, $\theta_{\text{sk}} = 0.0$ when the background skyrmions form an ordered checkerboard state and the driven skyrmion follows a 1D path along the x direction. For higher fillings, $\langle V \rangle$ and the magnitude of θ_{sk} gradually decrease.

The skyrmion locking to 1D motion at the $f = 1.0$ commensurate state is caused by the repulsion of the driven skyrmion from skyrmions trapped at the pinning sites. At commensurate fillings, the pinned skyrmions form an ordered structure that contains 1D easy flow paths for the driven skyrmion. These paths confine the driven skyrmion and prevent its motion from aligning with the angle induced by the skyrmion Hall effect. They also produce a peak in the velocity since the Magnus term rotates part of the repulsive force from the sides of the 1D channel into the direction of motion of the driven skyrmion. In contrast, at incommensurate fillings there are weak spots in the 1D confining potential that allow the skyrmion to escape from the confinement and move with a finite skyrmion Hall angle. In general, since skyrmion-skyrmion interactions strongly affect the motion of the driven skyrmion, by modifying the density of the background skyrmions we can change from a regime at commensuration in which the driven skyrmion is effectively moving over a periodic substrate to a regime just off commensuration where the driven skyrmion is moving over different levels of disorder. We can even consider strongly incommensurate regimes.

An alternative realization of this system would be a driven skyrmion moving over a periodic array of repulsive sites [48], which could be created using methods such as those described in Refs. [53,127]; however, this would only capture the $f = 1.0$ behavior. In principle, a series of samples could be fabricated in which repulsive sites are omitted or extra repulsive sites are added in order to mimic incommensurate fillings; however, the advantage of our system is that a wide range of commensurate and incommensurate states can be accessed using only a single sample by tuning the skyrmion density with a simple control parameter such as an external magnetic field.

In Figs. 4(a)–4(c), we plot $\langle V_x \rangle$, $\langle V_y \rangle$, $\langle V \rangle$, and θ_{sk} versus f for the system from Fig. 2 but with stronger dissipation of $\alpha_m/\alpha_d = 0.204$, where $\theta_{\text{sk}}^{\text{int}} = -11.54^\circ$. We find that θ_{sk} is equal to zero at $f = 1.0$ and $f = 2.0$, and is small in magnitude for all $f > 0.5$. There is still a strong peak in $\langle V_x \rangle$ and $\langle V \rangle$ at $f = 1.0$, with a smaller peak appearing at $f = 2.0$. In Figs. 4(d)–4(f), similar behavior appears at $\alpha_m/\alpha_d = 0.436$ with $\theta_{\text{sk}}^{\text{int}} = -21.9^\circ$, where there is a strong peak in $\langle V \rangle$ at $f = 1.0$.

The behavior of $\langle V_x \rangle$, $\langle V_y \rangle$, $\langle V \rangle$, and θ_{sk} versus f in a system with $\alpha_m/\alpha_d = 0.57$ and $\theta_{\text{sk}}^{\text{int}} = -30^\circ$ appears in Figs. 5(a)–5(c). There are peaks in $\langle V \rangle$ at $f = 1.0$, 2.0 , and 3.0 , coinciding with fillings for which $\theta_{\text{sk}} = 0^\circ$. Figures 5(d)–5(f) shows the same quantities for a sample with $\alpha_m/\alpha_d = 1.33$ and $\theta_{\text{sk}}^{\text{int}} = -53^\circ$. At the matching fillings, $\langle V_y \rangle$ has a dip in magnitude but does not drop completely to zero. There is a cusp in θ_{sk} to $\theta_{\text{sk}} = -4^\circ$ at $f = 1.0$, and another more rounded cusp appears at $f = 2.0$. For these parameters, there is no peak in $\langle V \rangle$ at $f = 1.0$, but there is a smaller peak

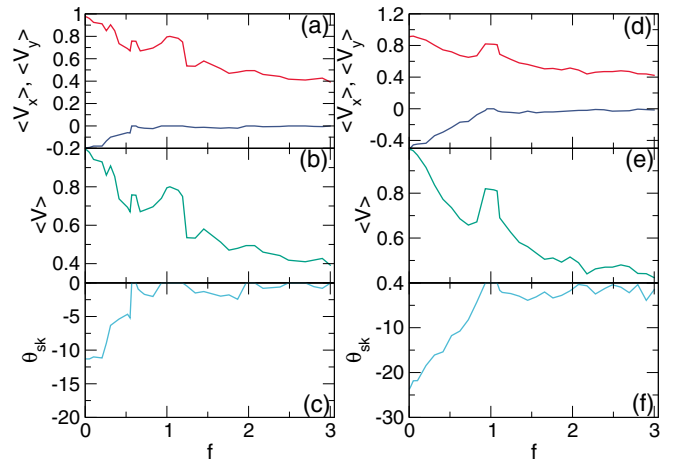


FIG. 4. Behavior under varied filling fraction f for the system from Fig. 2 with a square pinning array, $F_p = 0.25$, and $F_D = 1.0$, but with [(a)–(c)] $\alpha_m/\alpha_d = 0.204$ and $\theta_{\text{sk}}^{\text{int}} = -11.54^\circ$ and [(d)–(f)] $\alpha_m/\alpha_d = 0.436$ and $\theta_{\text{sk}}^{\text{int}} = -21.9^\circ$. (a,d) $\langle V_x \rangle$ (red) and $\langle V_y \rangle$ (blue) vs f . [(b) and (e)] $\langle V \rangle$ vs f . [(c) and (f)] θ_{sk} vs f .

at $f = 0.66$. In Fig. 5(e), we observe regions over which $\langle V \rangle > 1.0$, indicated by locations where the curve rises above the dashed line. This is a signature of a velocity boost produced by interactions with the background skyrmions and the pinning sites. In general, as the density increases, there are more collisions with the background skyrmions that increase the effective dissipative velocity; however, since the collisions can also contribute to the odd viscosity, there is a competition between the viscosity components. When the odd viscosity term dominates, the velocity boost effect can emerge [93,94].

For a sample with $\alpha_m/\alpha_d = 2.065$ and $\theta_{\text{sk}}^{\text{int}} = -64^\circ$, we plot $\langle V_x \rangle$, $\langle V_y \rangle$, $\langle V \rangle$, and θ_{sk} versus f in Figs. 6(a)–6(c). The

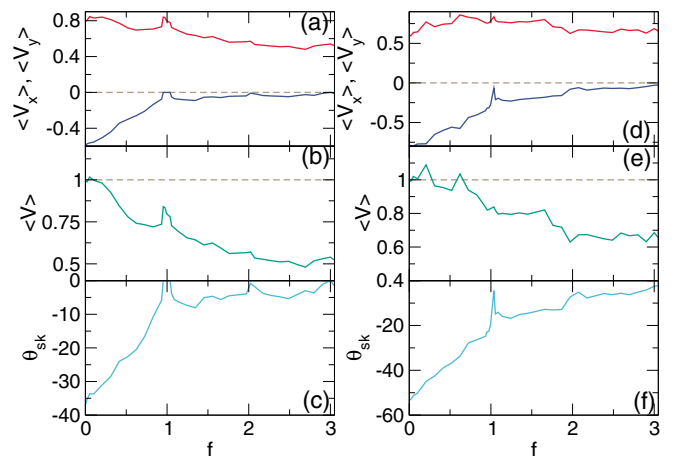


FIG. 5. Behavior under varied f for the system from Fig. 2 with a square pinning array, $F_p = 0.25$, and $F_D = 1.0$, but with [(a)–(c)] $\alpha_m/\alpha_d = 0.57$ and $\theta_{\text{sk}}^{\text{int}} = -30^\circ$ and [(d)–(f)] $\alpha_m/\alpha_d = 1.33$ and $\theta_{\text{sk}}^{\text{int}} = -53^\circ$. [(a) and (d)] $\langle V_x \rangle$ (red) and $\langle V_y \rangle$ (blue) vs f . [(b) and (e)] $\langle V \rangle$ vs f . [(c) and (f)] θ_{sk} vs f . The dashed lines in (b) and (e) are at $\langle V \rangle = 1.0$, showing that there is a small boost effect in panel (e) for $f < 1.0$.

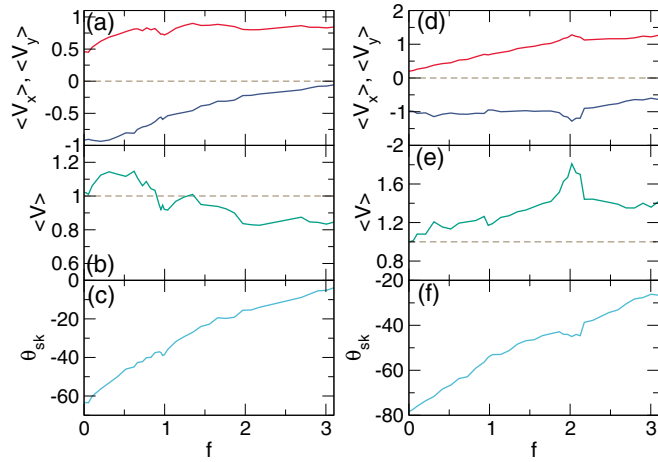


FIG. 6. Behavior under varied f for the system from Fig. 2 with a square pinning array, $F_p = 0.25$, and $F_D = 1.0$, but with [(a)–(c)] $\alpha_m/\alpha_d = 2.065$ and $\theta_{\text{sk}}^{\text{int}} = -64^\circ$ and [(d)–(f)] $\alpha_m/\alpha_d = 4.92$ and $\theta_{\text{sk}}^{\text{int}} = -78^\circ$. [(a) and (d)] $\langle V_x \rangle$ (red) and $\langle V_y \rangle$ (blue) vs f . [(b) and (e)] $\langle V \rangle$ vs f . [(c) and (f)] θ_{sk} vs f . The dashed lines in (b) and (e) indicate the value $\langle V \rangle = 1.0$; boost effects are present when $\langle V \rangle$ rises above this value.

peaks that appeared in $\langle V \rangle$ at $f = 1.0$ and $f = 2.0$ for lower α_m/α_d have not only disappeared, but there is now a dip in $\langle V \rangle$ at $f = 1.0$ accompanied by a small increase in the magnitude of θ_{sk} . A velocity boost appears over the entire range $0.1 < f < 1.0$, as indicated by the curve rising above the dashed $\langle V \rangle = 1.0$ line in Fig. 6(b). There is an increase in $\langle V_x \rangle$ over the same range of fillings since the boosted velocity is aligned with the driving or $+x$ direction, and when the Magnus force is large enough, the magnitude of the boost increases with decreasing magnitude of the skyrmion Hall angle θ_{sk} [93]. We plot the same quantities for a sample with $\alpha_m/\alpha_d = 4.92$ and $\theta_{\text{sk}}^{\text{int}} = -78^\circ$ in Figs. 6(d)–6(f). Here there is no large feature at $f = 1.0$; instead, strong peaks or dips appear in $\langle V_x \rangle$, $\langle V_y \rangle$ and $\langle V \rangle$ at $f = 2.0$. For this filling, $\theta_{\text{sk}} = -45^\circ$, indicating that the commensurate structure is directionally locked with one of the major symmetry angles of the pinning array. As f increases further, the magnitude of θ_{sk} resumes its decrease after passing through the locking step at $\theta_{\text{sk}} = -45^\circ$. At $f = 2.0$, the system forms an ordered checkerboard state with a well defined symmetry direction; however, away from $f = 2.0$, the structure becomes disordered again and the directional locking is lost. In Fig. 6(d), $\langle V_x \rangle$ increases with increasing f while the magnitude of $\langle V_y \rangle$ undergoes a moderate decrease. Figure 6(e) shows that a velocity boost is present over the entire range of f except at very small values of f , with the largest boost appearing at $f = 2.0$. At this filling, $\langle V \rangle \approx 1.8$, nearly twice as large as the expected velocity in the limit of a single skyrmion and no substrate.

Taken together, the results in this section indicate that commensuration effects can both reduce the skyrmion Hall angle and also speed up the skyrmion motion, two features that are desirable for applications. For values of α_m/α_d higher than what is shown here, we observe similar trends; however, as the relative strength of the damping term becomes small, the motion becomes increasingly disordered and fluid-like,

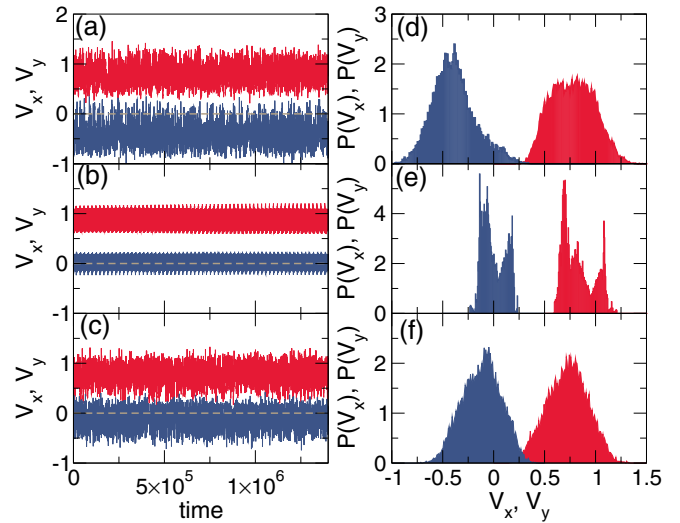


FIG. 7. Velocity fluctuation data for the system from Fig. 2 with a square pinning array, $F_p = 0.25$, $F_D = 1.0$, $\alpha_m/\alpha_d = 1.0$, and $\theta_{\text{sk}}^{\text{int}} = -45^\circ$ at [(a) and (d)] $f = 0.62$, [(b) and (e)] 1.0 , and [(c) and (f)] 1.14 . [(a)–(c)] Time series of the instantaneous velocities V_x (red) and V_y (blue). [(d)–(f)] The corresponding velocity distributions $P(V_x)$ (red) and $P(V_y)$ (blue). The distributions have a Gaussian character at $f = 0.62$ in (d) and $f = 1.14$ in (f) when the motion is disordered, but develop sharp peaks at $f = 1.0$ in (e) when the motion is periodic.

the curves become smooth, and the directional locking effects disappear. In addition, for values of f higher than those shown here, the velocity boost is eventually destroyed. For lower F_D and high fillings, a jamming effect can occur in which the driven skyrmion becomes pinned or jammed due to its strong interactions with the background skyrmions, similar to what is found in other active rheology systems [105,128].

A. Fluctuations and noise

We can also characterize the behavior of the commensurate and noncommensurate states using the fluctuation properties of the time series of the driven skyrmion velocity. In general, we find ordered motion at commensurate fillings for which $\theta_{\text{sk}} = 0^\circ$ and disordered motion at incommensurate fillings where θ_{sk} is finite. In Figs. 7(a)–7(c), we plot the time series of the instantaneous velocities V_x and V_y for the system in Fig. 2 with $\theta_{\text{sk}}^{\text{int}} = -45^\circ$. At $f = 0.62$ in Fig. 7(a), where $\theta_{\text{sk}} = -28^\circ$, the velocities fluctuate rapidly and, as shown in the corresponding velocity distribution plots $P(V_x)$ and $P(V_y)$ in Fig. 7(d), the distributions have a broadened Gaussian form that is characteristic of random fluctuations. At $f = 1.0$ in Figs. 7(b) and 7(e), the motion is periodic and $P(V_y)$ is centered at zero. Here the velocity distributions are non-Gaussian and have sharp features indicative of the repeated periodic motion. In Figs. 7(c) and 7(f) at $f = 1.14$, corresponding to the motion with $\theta_{\text{sk}} = -10^\circ$ illustrated in Fig. 3(b), the flow is once again random with Gaussian velocity distributions. We find similar behaviors for commensurate and incommensurate fillings at other values of α_m/α_d , including the $\langle V_y \rangle = 0$ states at $f = 1.0$ and $f = 2.0$ where the motion is periodic. For higher values of α_m/α_d such as $\alpha_m/\alpha_d = 1.33$ in Fig. 5(f),

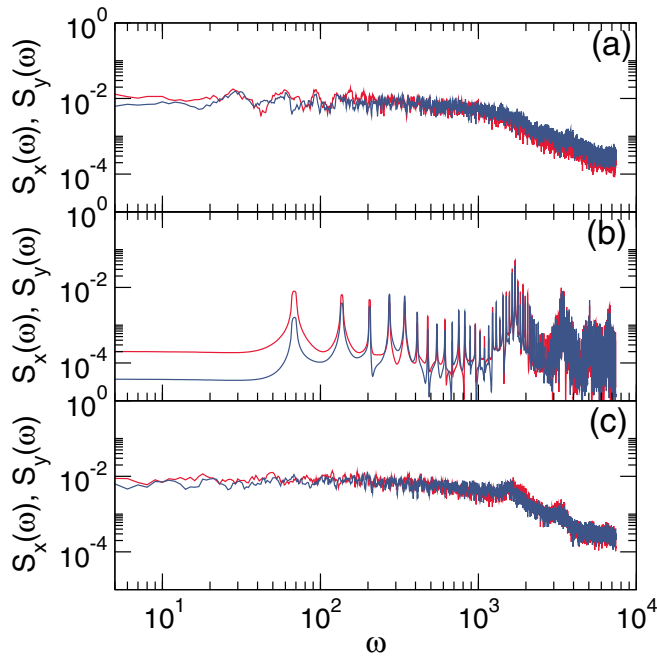


FIG. 8. The power spectra $S_x(\omega)$ (red) and $S_y(\omega)$ (blue) for the velocity time series V_x and V_y , respectively, in Fig. 7 from samples with a square pinning array, $F_p = 0.25$, $F_D = 1.0$, $\alpha_m/\alpha_d = 1.0$, and $\theta_{\text{sk}}^{\text{int}} = -45^\circ$. (a) $f = 0.62$. (b) $f = 1.0$, where there is a strong narrow band noise signature. (c) $f = 1.14$.

where θ_{sk} does not reach zero but is strongly reduced at $f = 1.0$ and $f = 2.0$, the motion is mostly periodic with occasional jumps in the transverse direction.

The skyrmion motion can also be characterized by examining the velocity noise, as considered in both simulations [52] and experiments [129]. From the time series in Fig. 7, we can extract the power spectrum $S_\alpha(\omega) = |\int V_\alpha(t)e^{-i\omega t} dt|^2$, where $\alpha = x, y$. In Fig. 8 we plot the power spectra from the time series of both V_x and V_y for the system in Fig. 7. At $f = 0.62$ in Fig. 8(a), there are no peaks in the power spectra, indicating that the motion is random, while at $f = 1.0$ in Fig. 8(b), there is a strong narrow band noise signal in the form of a sequence of peaks. In this case, there are two overlapping periodic signals. The first, at higher frequencies, arises from the periodic motions of the driven skyrmion as it interacts with the ordered commensurate pinned skyrmions. The second, at lower frequencies, is produced by a small number of defects that are present in the commensurate configuration, which generate a time-of-flight velocity signature. For the disordered motion at $f = 1.14$ in Fig. 8(c), the noise signature has a broad band character. There is a weak periodic signal at higher frequencies due to the low value of θ_{sk} at this filling, which causes the skyrmion to flow through an interstitial channel between two adjacent pinning rows with infrequent but roughly periodic hops occurring from one interstitial channel to the next.

In Fig. 9, we use the behavior of the transport curves and θ_{sk} to construct a dynamic phase diagram as a function of filling fraction f versus α_m/α_d for the system in Fig. 2. In the red region, the skyrmion moves strictly along the direction of drive and $\theta_{\text{sk}} = 0^\circ$. In the blue region, the skyrmion Hall

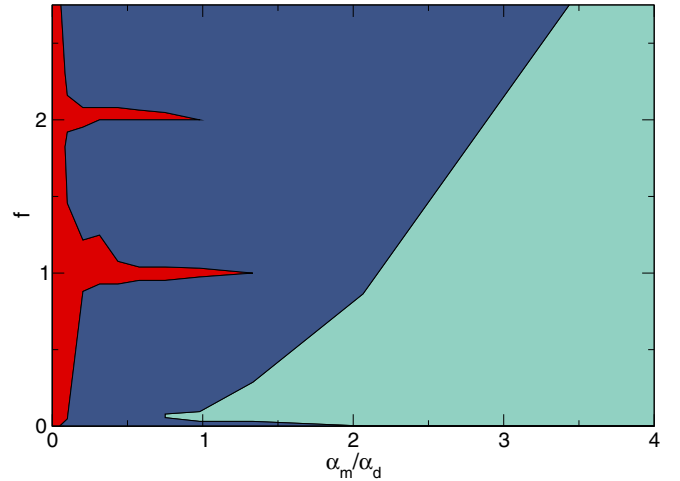


FIG. 9. Dynamic phase diagram as a function of filling fraction f vs α_m/α_d for the system in Fig. 2 with a square pinning array, $F_p = 0.25$, and $F_D = 1.0$ constructed using the features in the transport curves and the behavior of θ_{sk} . In the red region, $\theta_{\text{sk}} = 0^\circ$, a condition that extends out to higher α_m/α_d at commensurate fillings. In the blue region, θ_{sk} is finite but there is no velocity boost, while in the green region, θ_{sk} remains finite and a velocity boost appears.

angle is finite but there is no velocity boost, and in the green region, there is both a finite skyrmion Hall angle and a finite velocity boost. Near the commensurate conditions of $f = 1.0$ and $f = 2.0$, the window of zero skyrmion Hall angle extends out to larger values of α_m/α_d . For these same commensurate conditions, even when the value of θ_{sk} becomes finite, it is still suppressed relative to its value away from commensuration, a feature that is not illustrated in the plot. We note that the peaks in the velocity are the most persistent when the intrinsic skyrmion Hall angle is smaller than 45° , where $\alpha_m/\alpha_d < 1$. In contrast, the boost effect generally does not appear until $\theta_{\text{sk}}^{\text{int}} \geq 45^\circ$ or $\alpha_m/\alpha_d > 1$.

IV. VELOCITY FORCE CURVES

We next consider the effect of varying the driving force F_D on the driven particle in the system from Fig. 2. In Fig. 10(a), we plot $\langle V_x \rangle$ and $\langle V_y \rangle$ versus F_D at $f = 0.62$. There is a single depinning threshold at $F_D = 0.6$, above which motion occurs simultaneously in both directions. Figure 10(b) shows the corresponding θ_{sk} versus F_D , where $\theta_{\text{sk}} = 0^\circ$ at the depinning threshold. As F_D increases, the magnitude of θ_{sk} gradually increases until it approaches the intrinsic value $\theta_{\text{sk}}^{\text{int}} = -45^\circ$ at higher drives. In Fig. 10(c), $\langle V_x \rangle$ and $\langle V_y \rangle$ versus F_D for a sample with $f = 1.0$ reveal the presence of a two step depinning threshold. The first depinning transition occurs at $F_D = 0.55$, and for $0.55 < F_D < 1.25$ the motion is only along the x direction with $\theta_{\text{sk}} = 0^\circ$. The second depinning transition occurs at $F_D = 1.25$, above which finite motion in the y direction appears. In the corresponding plot of θ_{sk} versus F_D in Fig. 10(d), θ_{sk} is zero above the first depinning transition and begins to increase in magnitude above the second depinning transition. There are also several steps or plateaus in the velocity, including one with $\theta_{\text{sk}} \sim -27^\circ$ and another with $\theta_{\text{sk}} = -45^\circ$. These correspond to directional locking steps

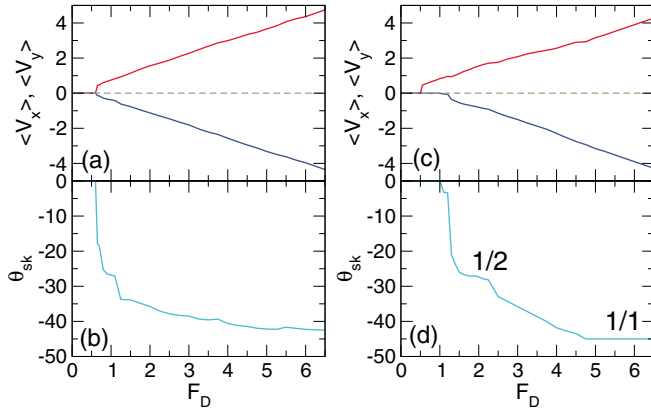


FIG. 10. (a) $\langle V_x \rangle$ (red) and $\langle V_y \rangle$ (blue) vs driving force F_D for the system from Fig. 2 with a square pinning array, $F_p = 0.25$, $\alpha_m/\alpha_d = 1.0$, and $\theta_{\text{sk}}^{\text{int}} = -45^\circ$ at a filling fraction of $f = 0.62$. (b) The corresponding θ_{sk} vs F_D . (c) $\langle V_x \rangle$ (red) and $\langle V_y \rangle$ (blue) vs F_D for the same system at $f = 1.0$, where there is a two step depinning process. (d) The corresponding θ_{sk} versus F_D contains two directional locking steps along the angles $\theta_{\text{sk}} = \arctan(1/2)$ and $\theta_{\text{sk}} = \arctan(1/1)$.

with $\theta_{\text{sk}} = \phi = \arctan(n/m)$. The $n/m = 1/2$ step has $\phi = \arctan(1/2) = -25.56^\circ$, while the $1/1$ step has $\phi = -45^\circ$.

In Fig. 11(a), we illustrate the skyrmion trajectories for the sample in Figs. 10(c) and 10(d) at a nonstep drive of $F_D = 2.75$, which is close to but not on the $1/2$ step. There is a combination of ordered and disordered motions, with regions in which the skyrmion translates by a distance $2a$ in the x direction and $-a$ in the y direction, combined with regions in which the skyrmion makes occasional jumps in other directions. Figure 11(b) shows the same system at $F_D = 6.0$ on the $1/1$ step, where the skyrmion moves in an orderly periodic fashion strictly along -45° .

In Figs. 12(a), we plot the time series of V_y on the $1/1$ step at $F_D = 6.0$ in the system from Figs. 10(c) and 10(d), while in Fig. 12(c) we show the corresponding Fourier transform $F(\omega) = \int V_y e^{-i\omega t} dt$, where there is a strong narrow band signal. The time series of V_y for a nonstep region at $F_D = 3.25$

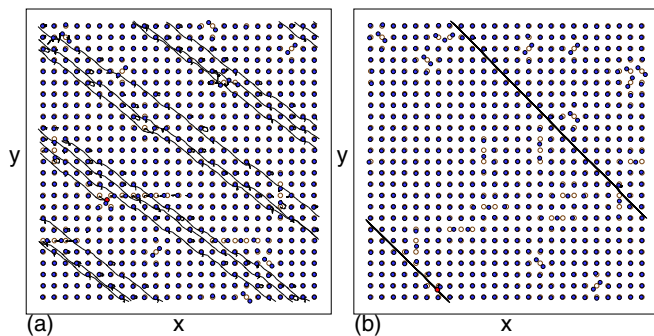


FIG. 11. Images of samples containing a square pinning lattice showing background skyrmions (blue filled circles), pinning site locations (brown circles), the driven skyrmion (red filled circle), and the skyrmion trajectories during a fixed time window for the system in Figs. 10(c) and 10(d) with $F_p = 0.25$, $\alpha_m/\alpha_d = 1.0$, and $\theta_{\text{sk}}^{\text{int}} = -45^\circ$ at a filling fraction of $f = 1.0$. (a) $F_D = 2.75$ near the $1/2$ step. (b) $F_D = 6.0$ along the $1/1$ step.

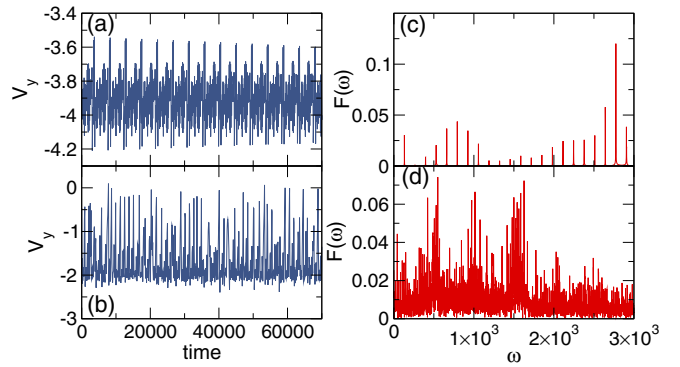


FIG. 12. [(a) and (b)] The time series of V_y and [(c) and (d)] its corresponding Fourier transform $F(\omega)$ for the system from Figs. 10(c) and 10(d) with a square pinning array, $F_p = 0.25$, $\alpha_m/\alpha_d = 1.0$, and $\theta_{\text{sk}}^{\text{int}} = -45^\circ$ at a filling fraction of $f = 1.0$. [(a) and (b)] $F_D = 6.0$ on the $1/1$ locking step where the motion is periodic. [(c) and (d)] A nonstep region at $F_D = 3.25$ where the flow is more disordered and the peaks in $F(\omega)$ are broadened.

with partially periodic motion appears in Fig. 12(b), and the broadened signature of the corresponding $F(\omega)$ is shown in Fig. 12(d). In general, as a function of increasing F_D we find that in regimes of directional locking where there are steps in θ_{sk} , the periodic motion produces narrow band velocity noise, while in regimes where no steps are present, the motion is more disordered and the velocity noise is either broad band or contains weakly periodic signals.

For individual skyrmions moving over a square substrate in the absence of background skyrmions, previous work showed that the velocity-force curve and skyrmion Hall angle exhibit a series of steps corresponding to directional locking centered on the values $\theta_{\text{sk}} = \arctan(n/m)$ with m, n integer [48]. For the active rheology situation we consider here, due to the large number of collisions the driven skyrmion experiences with background skyrmions, only the most prominent locking steps are visible, as illustrated in Fig. 10(d). In general, higher order directional locking only occurs at the commensurate conditions of $f = 1.0$ and $f = 2.0$, but there is some weaker higher order locking at some incommensurate fillings as well. The number of accessible steps also depends on the value of α_m/α_d ; as this quantity becomes larger, a greater number of steps beyond $1/1$ can be accessed.

In Figs. 13(a) and 13(b), we plot $\langle V_x \rangle$, $\langle V_y \rangle$, and θ_{sk} versus F_D for the system from Fig. 10 at a filling fraction of $f = 1.1392$. The locking step features are reduced or absent, while $\langle V_x \rangle$ and $\langle V_y \rangle$ both become finite at a single depinning transition near $F_D = 0.5$. Figures 13(c) and 13(d) shows the same quantities for $f = 2.0$, where there is a two step depinning transition in which $\langle V_x \rangle$ becomes finite at $F_D = 0.5$ and $\langle V_y \rangle$ does not become finite until $F_D = 1.15$. There is a reduced $1/2$ locking step, but the $1/1$ locking step remains robust. In Fig. 14(a), we illustrate the skyrmion trajectories in a subsection of the sample at $F_D = 6.0$ on the $1/1$ locking step, where the driven skyrmion moves at -45° through an interstitial channel in the checkerboard lattice formed by the background skyrmions. The $1/1$ step is associated with a cusp in $\langle V_x \rangle$ and $\langle V_y \rangle$ as indicated in Fig. 13(c). For driving

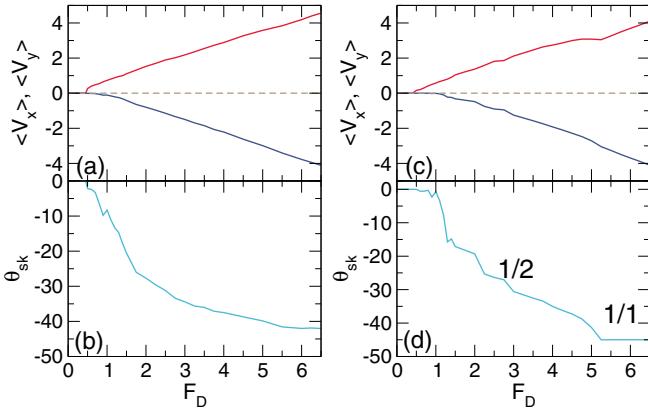


FIG. 13. (a) $\langle V_x \rangle$ (red) and $\langle V_y \rangle$ (blue) vs F_D for the system from Fig. 2 with a square pinning array, $F_p = 0.25$, $\alpha_m/\alpha_d = 1.0$, and $\theta_{sk}^{int} = -45^\circ$ at $f = 1.1392$. (b) The corresponding θ_{sk} versus F_D . (c) $\langle V_x \rangle$ (red) and $\langle V_y \rangle$ (blue) vs F_D for the same system at $f = 2.0$ where there is a two step depinning process. (d) The corresponding θ_{sk} versus F_D contains two directional locking steps at $1/1$ and $1/2$.

individual skyrmions over a periodic substrate in the absence of background skyrmions, similar cusps in the velocity-force curves appear at several of the transitions into and out of the directional locking steps [48]. Figure 14(b) shows the same system in a nonstep region at $F_D = 3.25$, where the motion is more disordered and θ_{sk} is smaller in magnitude.

V. VARIED PINNING STRENGTH

We next consider the effect of increasing the pinning strength for the system in Fig. 2 with fixed $\alpha_m/\alpha_d = 1.0$ and $F_D = 1.0$. In Figs. 15(a)–15(c), we plot $\langle V_x \rangle$, $\langle V_y \rangle$, $\langle V \rangle$, and θ_{sk} versus f for a sample with $F_p = 0.125$, which is half the value of F_p used in Fig. 2. The general trends remain unchanged, with the magnitude of θ_{sk} dropping to zero at $f = 1.0$ and reaching a value close to zero at $f = 2.0$. Figures 15(d)–15(f) shows the same quantities in a sample with stronger pinning, $F_p = 0.5$. The shapes of the curves remain similar to those at

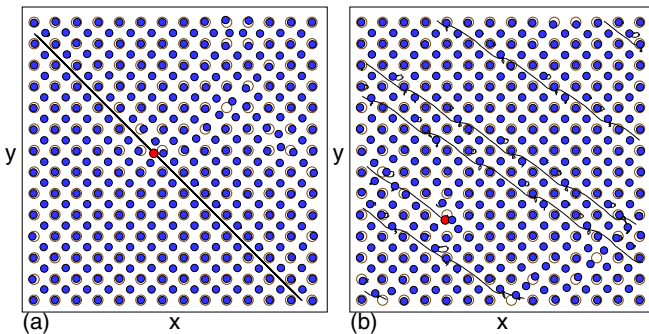


FIG. 14. Images of portions of samples containing a square pinning lattice showing background skyrmions (blue filled circles), pinning site locations (brown circles), the driven skyrmion (red filled circle), and the skyrmion trajectories during a fixed time window for the system in Figs. 13(c) and 13(d) with $F_p = 0.25$, $\alpha_m/\alpha_d = 1.0$, and $\theta_{sk}^{int} = -45^\circ$ at $f = 2.0$. (a) $F_D = 6.0$ on the $1/1$ step. (b) $F_D = 3.25$ in a nonstep region.

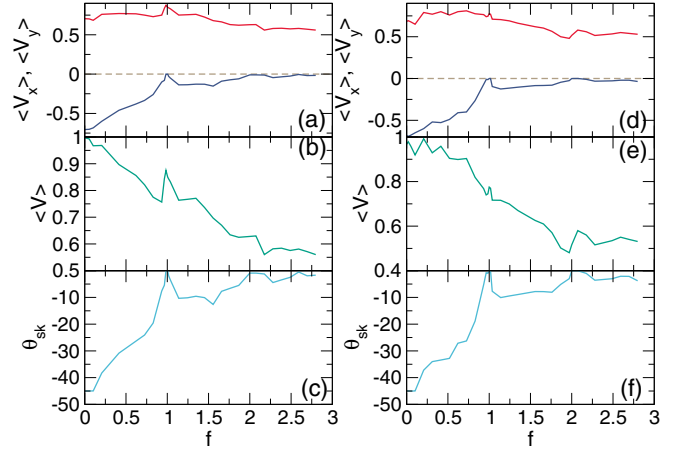


FIG. 15. Behavior under varied filling fraction f for the system shown in Fig. 2 with a square pinning array, $\alpha_m/\alpha_d = 1.0$, $\theta_{sk}^{int} = -45^\circ$, and $F_D = 1.0$. [(a) and (d)] $\langle V_x \rangle$ (red) and $\langle V_y \rangle$ (blue) vs f . [(b) and (e)] $\langle V \rangle$ vs f . [(c) and (f)] θ_{sk} vs f . The pinning strength is [(a)–(c)] $F_p = 0.125$ and [(d)–(f)] 0.5 .

lower F_p , but there is now a finite window of f near $f = 2.0$ where $\theta_{sk} = 0^\circ$.

In Figs. 16(a)–16(c), we plot $\langle V_x \rangle$, $\langle V_y \rangle$, $\langle V \rangle$, and θ_{sk} versus f for the same system in Fig. 15 but at stronger pinning of $F_p = 0.625$. There are now regions, such as near $f = 1.0$, where the system is pinned. There are also extended regions near $f = 2.0$ and $f = 3.0$ where θ_{sk} is close to zero. The pinned phase arises from the interaction between the driven skyrmion and the pinning sites, which occurs both directly when the driven skyrmion encounters a pinning site, and indirectly when the driven skyrmion experiences a repulsion from a pinned skyrmion. At low f , the driven particle has only direct interactions with the pinning sites, and as long as $F_D/F_p > 1.0$, it will not become pinned. At large f , all of the pinning sites are occupied by background skyrmions and

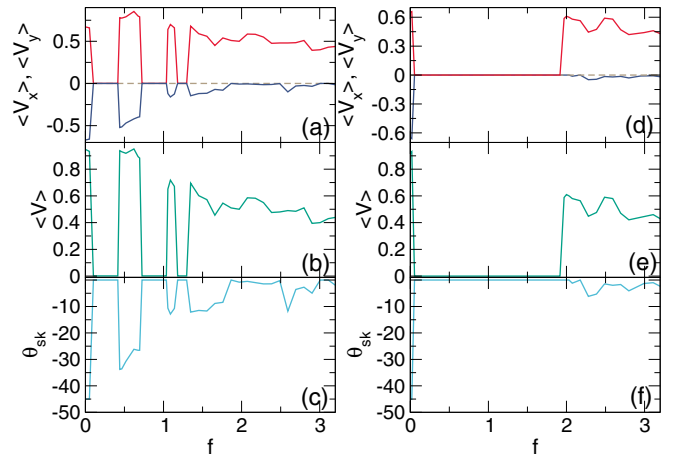


FIG. 16. Behavior under varied filling fraction f for the system from Fig. 2 with a square pinning array, $\alpha_m/\alpha_d = 1.0$, $\theta_{sk}^{int} = -45^\circ$, and $F_D = 1.0$. [(a) and (d)] $\langle V_x \rangle$ (red) and $\langle V_y \rangle$ (blue) vs f . [(b) and (e)] $\langle V \rangle$ vs f . [(c) and (f)] θ_{sk} vs f . The pinning strength is [(a)–(c)] $F_p = 0.625$ and [(d)–(f)] 0.75 .

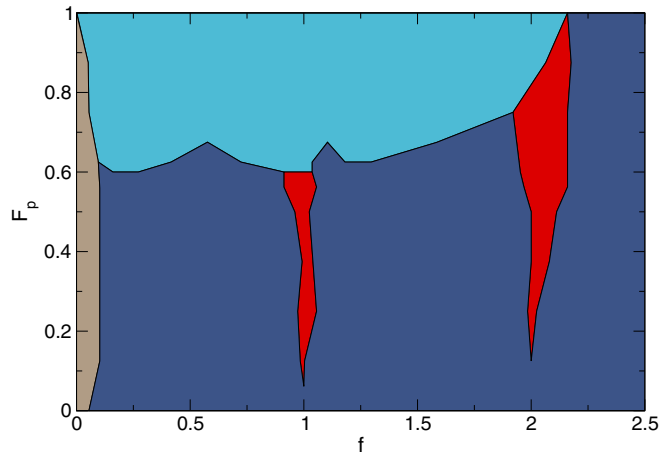


FIG. 17. Dynamic phase diagram as a function of pinning strength F_p and filling fraction f for the system in Figs. 15 and 16 with a square pinning array, $F_D = 1.0$, and $\alpha_m/\alpha_d = 1.0$. The system is pinned in the light blue region, moving with $\theta_{sk} = 0.0^\circ$ in the red region, moving with $\theta_{sk} = -45^\circ$ in the brown region, and moving with finite θ_{sk} and no velocity boost in the dark blue region.

the driven skyrmion never encounters a pinning site directly; however, for certain incommensurate fillings at which the positions of the background skyrmions become disordered, the driven skyrmion can become pinned via interactions with skyrmions located at pinning sites. The plots of $\langle V_x \rangle$, $\langle V_y \rangle$, $\langle V \rangle$, and θ_{sk} versus f in Figs. 16(d)–16(f) for the same system at $F_p = 0.75$ show that motion only occurs for $f < 0.05$ and $f > 2.0$ with a broad pinned window appearing in between those fillings, while the magnitude of θ_{sk} remains below 10° for the higher fillings.

Using the features in the transport curves and θ_{sk} , in Fig. 17 we construct a dynamic phase diagram as a function of F_p versus f for the system in Figs. 15 and 16 with $\alpha_m/\alpha_d = 1.0$ and $F_D = 1.0$. A large pinned region appears at larger F_p . There are some smaller pinned regimes (not shown) above $f = 2.1$. The intervals of pinning also depend strongly on F_D . When $\theta_{sk} \approx 0^\circ$, the motion is locked to the x direction, shown as red regions. For low f where there are few interactions with background skyrmions, the brown region indicates that the motion is locked to $\theta_{sk} = 45^\circ$. At these low values of f , pinned states occur only when $F_p > F_D = 1.0$. In the blue region, θ_{sk} is finite and there is no boost effect. Near the border between the flowing and pinned regimes, there are some windows of stick-slip motion, which produce $1/f$ velocity fluctuation noise and a bimodal velocity distribution with a peak at $\langle V \rangle = 0.0$ and a second peak at higher velocities.

We next consider a sample with strong pinning of $F_p = 0.75$ and $F_D = 1.0$ where we vary α_m/α_d . In Fig. 18(a), we plot $\langle V_x \rangle$ and $\langle V_y \rangle$ versus f for a system with $\alpha_m/\alpha_d = 0.1$ and $\theta_{sk}^{int} = -5.74^\circ$. In this case, $\langle V_y \rangle = 0$ over the entire range of f measured. There are two pinned intervals with $\langle V_x \rangle = 0$ at $0.075 < f < 0.92$ and $1.6 < f < 2.07$. For low f , the driven skyrmion moves along the pinning rows in the x direction. As f increases, the driven skyrmion begins to collide with other skyrmions and becomes pinned by the combination of the pinning and the interactions with the background skyrmions.

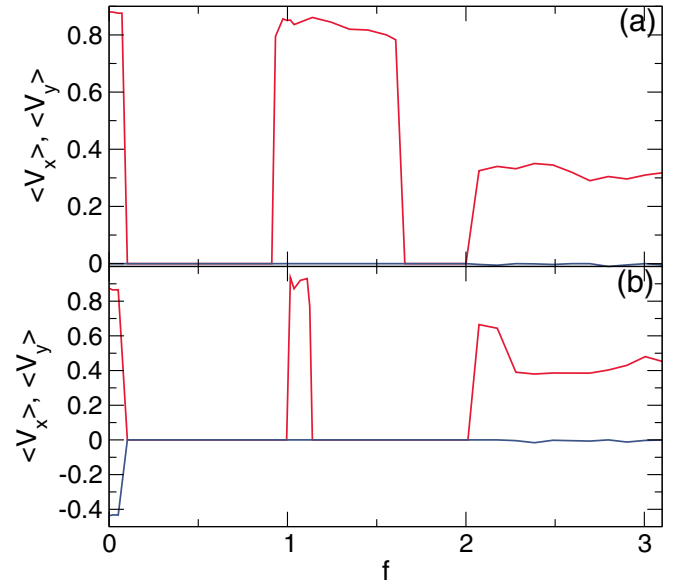


FIG. 18. $\langle V_x \rangle$ (red) and $\langle V_y \rangle$ (blue) versus f for a system with a square pinning array, $F_p = 0.75$, and $F_D = 1.0$. (a) $\alpha_m/\alpha_d = 0.1$ and $\theta_{sk}^{int} = -5.74^\circ$. (b) $\alpha_m/\alpha_d = 0.5$ and $\theta_{sk}^{int} = -30^\circ$.

Near $f = 1.0$ where the system is more ordered, the driven skyrmion channels along the x direction between the pinned skyrmions. Near $f = 0.8$, the background skyrmions are disordered enough that the driven skyrmion trajectory begins to divert into the y direction, but the driven skyrmion quickly becomes trapped among the background skyrmions. For $f > 2.0$, there are regions where the driven skyrmion depins and shepherds some of the background skyrmions along the x direction. Figure 18(b) shows $\langle V_x \rangle$ and $\langle V_y \rangle$ for a sample with $\alpha_m/\alpha_d = 0.58$ and $\theta_{sk}^{int} = -30^\circ$. For low f , the skyrmion Hall angle is finite. There is also a reduced window near $f = 1.0$ where the driven skyrmion channels along the x direction. Figure 18 demonstrates that increasing the Magnus component of the dynamics enhances the effectiveness of the pinning, a behavior opposite from what is typically observed in systems with random pinning [25]. The high Magnus force causes the driven skyrmion to attempt to move partially in the y direction rather than strictly along the x direction, and since the direction of motion no longer coincides with a symmetry direction of the pinning lattice, encounters with pinning and pinned skyrmions happen more frequently and increase the effectiveness of the pinning.

In Figs. 19(a)–19(c), we plot $\langle V_x \rangle$, $\langle V_y \rangle$, $\langle V \rangle$, and θ_{sk} versus f for a sample with $\alpha_m/\alpha_d = 2.06$ and $\theta_{sk}^{int} = -64.15^\circ$. From $0.41 < f < 1.08$, there is an unpinned region with motion locked to -45° , as indicated by the 1/1 label in Fig. 19(c). There is a pinned region for $1.08 < f < 2.16$ followed by another region in which motion occurs in both the x and y directions. Notice that when $f = 0$, $\langle V_x \rangle = 0.44$, but that in the range $0.41 < f < 1.0$, $\langle V_x \rangle \approx 0.9$, indicating a substantial boost of the velocity in the direction of driving. There is also a boost in the overall velocity for $1.08 < f < 2.16$, as shown in Fig. 19(b) where $\langle V \rangle$ rises above the dashed line marking $\langle V \rangle = 1.0$. Figures 19(d)–19(f) shows $\langle V_x \rangle$, $\langle V_y \rangle$, $\langle V \rangle$, and θ_{sk} versus f for a sample with $\alpha_m/\alpha_d = 3.04$ and $\theta_{sk}^{int} = -71.8^\circ$.

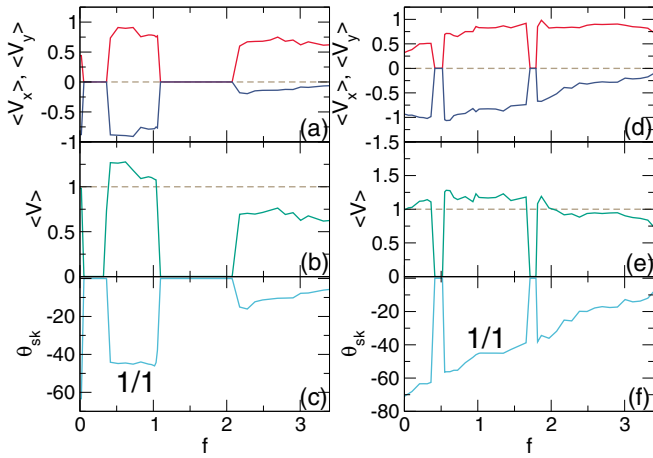


FIG. 19. Behavior under varied filling fraction f for a system with a square pinning array, $F_p = 0.75$, and $F_D = 1.0$. [(a) and (d)] $\langle V_x \rangle$ (red) and $\langle V_y \rangle$ (blue) vs f . [(b) and (e)] $\langle V \rangle$ vs f . [(c) and (f)] θ_{sk} vs f . [(a)–(c)] $\alpha_m/\alpha_d = 2.06$ and $\theta_{sk}^{\text{int}} = -64.15^\circ$. [(d)–(f)] $\alpha_m/\alpha_d = 3.04$ and $\theta_{sk}^{\text{int}} = -71.8^\circ$.

The pinned regions are reduced in width and occur away from the commensurate fillings. There is still directional locking to $\theta_{sk} = -45^\circ$ near $f = 1.0$, as indicated in Fig. 19(f) by the 1/1 label, and the velocity boosted regime in Fig. 19(e) is more extended.

In Figs. 20(a)–20(c), we plot $\langle V_x \rangle$, $\langle V_y \rangle$, $\langle V \rangle$, and θ_{sk} versus f for a system with $\alpha_m/\alpha_d = 4.39$ and $\theta_{sk}^{\text{int}} = -77.16^\circ$. There is a single pinned region near $f = 0.5$ and a peak in the magnitude of $\langle V_x \rangle$, $\langle V_y \rangle$, and $\langle V \rangle$ at $f = 2.0$, but there is no peak near $f = 1.0$. The peak near $f = 2.0$ falls at the end of an extended window of locking to -45° , shown as the 1/1 step in θ_{sk} in Fig. 20(c). Over most of the range of f shown, there is a strong velocity boost in $\langle V \rangle$, as indicated by $\langle V \rangle$ running above the $\langle V \rangle = 1.0$ line in Fig. 20(b). Figures 20(d)–20(f) shows $\langle V_x \rangle$, $\langle V_y \rangle$, $\langle V \rangle$, and θ_{sk} for a sample with $\alpha_m/\alpha_d =$

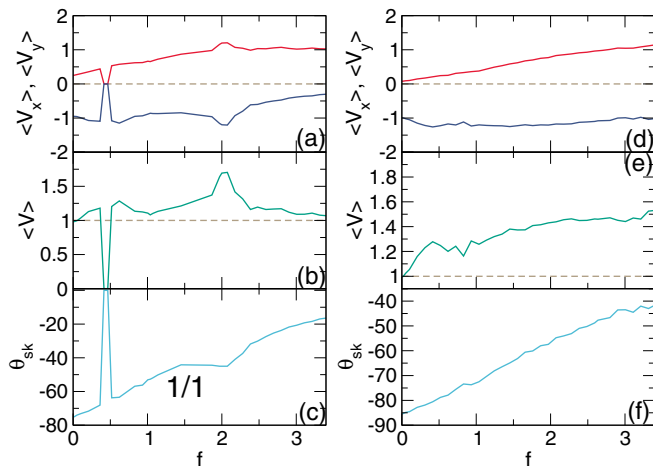


FIG. 20. Behavior under varied filling fraction f for a system with a square pinning array, $F_p = 0.75$, and $F_D = 1.0$. [(a) and (d)] $\langle V_x \rangle$ (red) and $\langle V_y \rangle$ (blue) vs f . [(b) and (e)] $\langle V \rangle$ vs f . [(c) and (f)] θ_{sk} versus f . [(a)–(c)] $\alpha_m/\alpha_d = 4.39$ and $\theta_{sk}^{\text{int}} = -77.16^\circ$. [(d)–(f)] $\alpha_m/\alpha_d = 13.28$ and $\theta_{sk}^{\text{int}} = -85.7^\circ$.

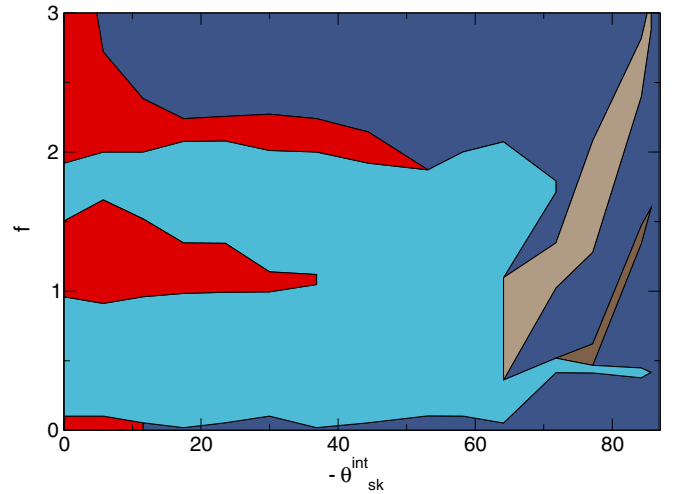


FIG. 21. Dynamic phase diagram as a function of filling fraction f versus intrinsic skyrmion Hall angle $-\theta_{sk}^{\text{int}}$ for the system from Figs. 18–20 with a square pinning array, $F_p = 0.75$, and $F_D = 1.0$. The pinned region is light blue, the red region is motion with $\theta_{sk} = 0^\circ$, the brown region is motion with $\theta_{sk} = -45^\circ$, the dark brown region is motion with $\theta_{sk} = \arctan(1/2)$, and the dark blue region is motion with finite θ_{sk} . Regions with and without velocity boost are not distinguished in this diagram.

13.28 and $\theta_{sk}^{\text{int}} = -85.7^\circ$, where there is no longer a pinned phase and only a small 1/1 locking step appears near $f = 3.0$. Here the magnitude of θ_{sk} decreases nearly monotonically with increasing f , while $\langle V \rangle$ shows an increasing velocity boost as f becomes larger. For large Magnus forces such as this, the dynamics become increasingly disordered, destroying the directional locking.

From the features in the transport curves and the behavior of θ_{sk} for the system in Figs. 18–20, we construct a dynamic phase diagram as a function of f versus $-\theta_{sk}^{\text{int}}$ in Fig. 21. We highlight the pinned phase, locking to the x direction with $\theta_{sk} = 0^\circ$, locking to $\theta_{sk} = -45^\circ$ or the 1/1 direction, locking to $\theta_{sk} = \arctan(1/2)$ or the 1/2 direction, and motion at a finite skyrmion Hall angle. No distinction is made between regions with and without a velocity boost in this figure. For $-\theta_{sk}^{\text{int}} < 45^\circ$, there are extended regions of locking in the x -direction, while the additional directional locking effects appear only for higher Magnus forces with $-\theta_{sk}^{\text{int}} > 60^\circ$. Near $f = 1.0$ and 2.0 , we find extended regions where $\theta_{sk} = 0^\circ$. There are extended regions of velocity boosting (not shown) which appear when $-\theta_{sk}^{\text{int}} > 45^\circ$.

VI. TRIANGULAR PINNING ARRAYS

If the square pinning array is replaced with a triangular pinning array, similar behavior occurs. In Figs. 22(a)–22(c), we plot $\langle V_x \rangle$, $\langle V_y \rangle$, $\langle V \rangle$, and θ_{sk} versus f for a sample with triangular pinning, $F_p = 0.5$, $F_D = 1.0$, $\alpha_m/\alpha_d = 1.0$, and $\theta_{sk}^{\text{int}} = -45.0^\circ$. Here θ_{sk} goes to zero at $f = 1.0$ but not at $f = 2.0$. For a triangular pinning array, the background skyrmions form a commensurate triangular lattice at $f = 1.0$; however, at $f = 2.0$ the skyrmions form a honeycomb structure rather than a triangular lattice. A similar structure has been observed

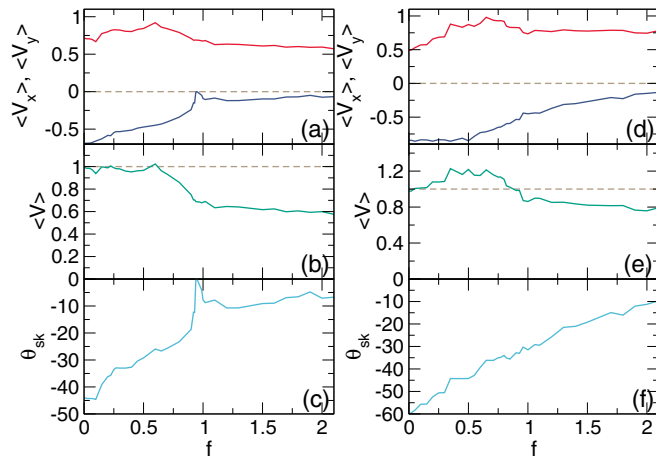


FIG. 22. Behavior under varied filling fraction f for a system with a triangular pinning array, $F_p = 0.5$, and $F_D = 1.0$. [(a) and (d)] $\langle V_x \rangle$ (red) and $\langle V_y \rangle$ (blue) vs f . [(b) and (e)] $\langle V \rangle$ vs f . [(c) and (f)] θ_{sk} vs f . [(a)–(c)] $\alpha_m/\alpha_d = 1.0$ and $\theta_{sk}^{int} = -45^\circ$. [(d)–(f)] $\alpha_m/\alpha_d = 1.73$ and $\theta_{sk}^{int} = -60^\circ$.

for superconducting vortices on a 2D triangular pinning array [73]. Since the honeycomb arrangement is less stable than the triangular arrangement, the background skyrmions are not as strongly pinned at $f = 2.0$ compared to $f = 1.0$, and there is less reduction of the drag on the driven skyrmion at $f = 2.0$. Figures 22(d)–22(f) shows $\langle V_x \rangle$, $\langle V_y \rangle$, and $\langle V \rangle$ versus f for the same sample at $\alpha_m/\alpha_d = 1.73$ and $\theta_{sk}^{int} = -60^\circ$, where the skyrmion Hall angle does not show any feature at $f = 1.0$. There is a small velocity boost for $f < 1.0$, as indicated by the excursion of $\langle V \rangle$ above the value $\langle V \rangle = 1.0$ in Fig. 21(e).

In Figs. 23(a)–23(c), we plot $\langle V_x \rangle$, $\langle V_y \rangle$, $\langle V \rangle$, and θ_{sk} versus f for a triangular pinning system with $\alpha_m/\alpha_d = 0.374$ and $\theta_{sk}^{int} = -20.5^\circ$. There is a pinned region near $f = 0.4$ along with a region of $\theta_{sk} = 0.0^\circ$ centered at $f = 1.0$ that coincides with a peak in the magnitudes of $\langle V_x \rangle$ and $\langle V_y \rangle$.

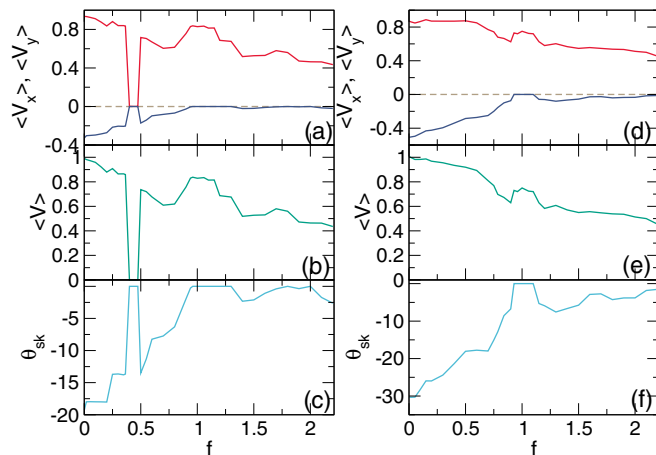


FIG. 23. Behavior under varied filling fraction f for a system with a triangular pinning array, $F_p = 0.5$, $F_D = 1.0$, and $n_p = 0.4882$. [(a) and (d)] $\langle V_x \rangle$ (red) and $\langle V_y \rangle$ (blue) vs f . [(b) and (e)] $\langle V \rangle$ vs f . [(c) and (f)] θ_{sk} vs f . [(a)–(c)] $\alpha_m/\alpha_d = 0.374$ and $\theta_{sk}^{int} = -20.5^\circ$. [(d)–(f)] $\alpha_m/\alpha_d = 0.658$ and $\theta_{sk}^{int} = -33.4^\circ$.

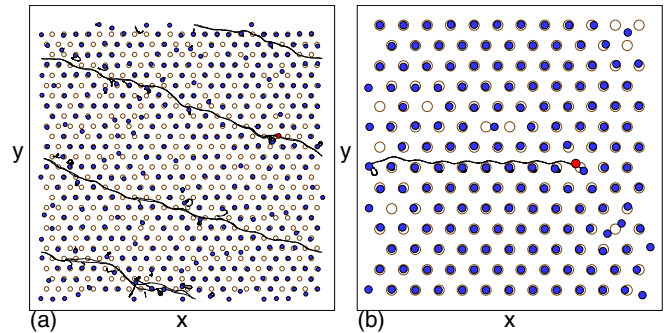


FIG. 24. Images of samples containing a triangular pinning lattice showing background skyrmions (blue filled circles), pinning site locations (brown circles), the driven skyrmion (red filled circle), and the skyrmion trajectories during a fixed time window for the system in Figs. 22(a)–22(c) with $F_p = 0.5$, $F_D = 1.0$, $\alpha_m/\alpha_d = 1.0$, and $\theta_{sk}^{int} = -45^\circ$. (a) $f = 0.6$. (b) A portion of the sample at $f = 1.0$, where the motion is only along the x direction.

Figures 23(d)–23(f) shows the same quantities in a sample with $\alpha_m/\alpha_d = 0.658$ and $\theta_{sk}^{int} = -33.4^\circ$, where a peak appears in $\langle V_x \rangle$ and $\langle V \rangle$ for $f = 1.0$. We do not see the same commensurate effects at $f = 2.0$ due to the honeycomb ordering.

Figure 24(a) illustrates the skyrmion trajectories for the system in Figs. 22(a)–22(c) at $f = 0.6$ where the skyrmion motion is along $\theta_{sk} \approx -18^\circ$. The driven skyrmion interacts both directly with the pinning sites and with the background skyrmions, and its trajectory is disordered. In Fig. 23(b), the same system at $f = 1.0$ exhibits channeling motion along the $\theta_{sk} = 0^\circ$ symmetry direction of the pinning array.

VII. THERMAL EFFECTS

Up to this point, we have not considered thermal fluctuations. In general, we expect our results to remain robust for temperature regimes where the driven skyrmion motion is confined to a 1D channel and the skyrmions in the pinning sites remain pinned. To test this, we measure the skyrmion Hall angle in a system with a square pinning array, $F_p = 0.5$, $\theta_{sk}^{int} = 45^\circ$, and $F_D = 0.7$. The temperature is added using Langevin kicks with the properties $\langle F_i^T(t) \rangle = 0$ and $\langle F_i^T(t) F_j^T(t') \rangle = 2\eta k_B T \delta_{ij} \delta(t - t')$ [88]. In Fig. 25, we plot $\theta_{sk} = \arctan(\langle V_y \rangle / \langle V_x \rangle)$ versus F^T for samples with $\alpha_m/\alpha_d = 1.0$ at fillings of $f = 0.7248$, 1.0 , and 1.45 . For the commensurate filling of $f = 1.0$, the skyrmion Hall angle starts at $\theta_{sk} = 0$ when $F^T = 0$ and rapidly increases in magnitude with increasing F^T . For the incommensurate fillings $f = 0.7248$ and $f = 1.45$, θ_{sk} remains roughly constant as F^T varies. The background skyrmions remain pinned when $F^T < 2.0$ but begin to hop out of the pinning sites once $F^T > 2.0$. The periodic background skyrmion lattice that appears when $f = 1.0$ becomes disordered by the onset of skyrmion hopping, and the behavior above but near $F^T = 2.0$ is nearly indistinguishable from that found for the incommensurate filling of $f = 1.45$. The magnitude of θ_{sk} is larger for $f = 1.0$ than for $f = 1.45$ at large thermal fluctuations of $F^T = 5.0$ where the system acts more like a fluid than a solid. Since the skyrmion density is higher at $f = 1.45$, there are more frequent collisions between the driven skyrmion and the background skyrmions, leading to

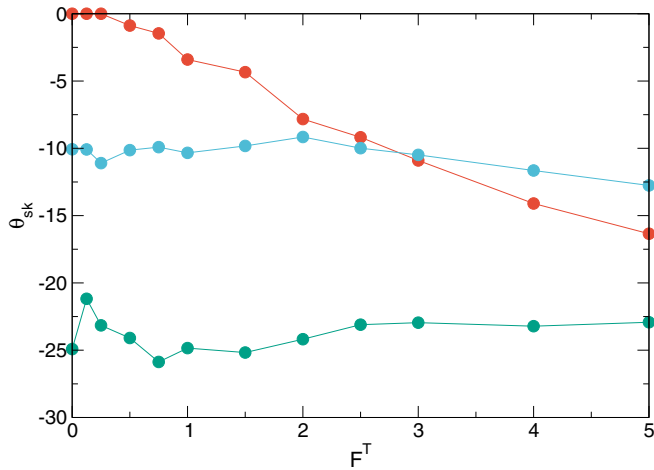


FIG. 25. Behavior of θ_{sk} as a function of thermal fluctuation magnitude F^T in a system with a square pinning array, $F_p = 0.5$, $\alpha_m/\alpha_d = 1.0$, $\theta_{\text{sk}}^{\text{int}} = -45^\circ$ and $F_D = 0.7$ at different filling fractions $f = 0.7248$ (green), 1.0 (red), and 1.45 (blue). When $F^T > 2.0$, the pinned skyrmions start to hop out of the pinning sites.

the reduction of the magnitude of the skyrmion Hall angle. In Fig. 26, we illustrate the skyrmion trajectories at $F^T = 5.0$ in the $f = 1.0$ sample where the thermal fluctuations have disordered the commensurate configuration of the background skyrmions.

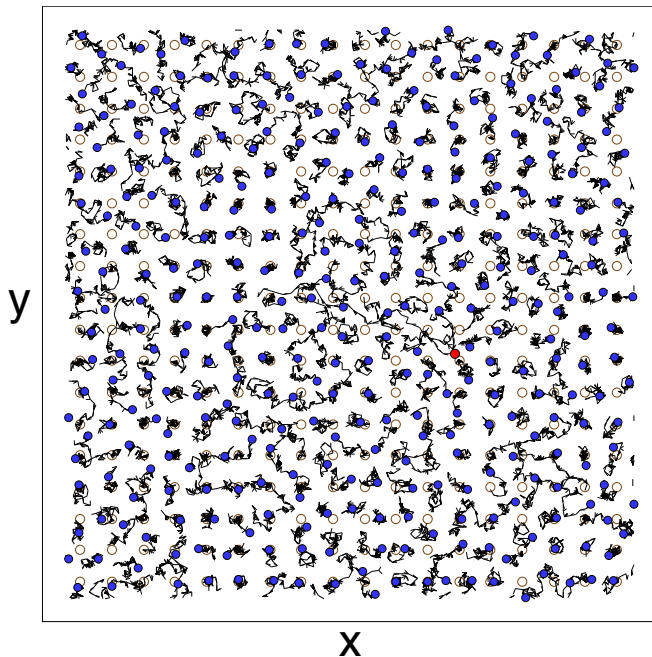


FIG. 26. Image of a sample containing a square pinning lattice showing background skyrmions (blue filled circles), pinning site locations (brown circles), the driven skyrmion (red filled circle), and the skyrmion trajectories during a fixed time window for the system in Fig. 25 with $F_p = 0.5$, $\alpha_m/\alpha_d = 1.0$, $\theta_{\text{sk}}^{\text{int}} = -45^\circ$, $F_D = 0.7$, and $f = 1.0$ under finite thermal fluctuations with $F^T = 5.0$. The ordered commensurate lattice is destroyed by the thermal fluctuations.

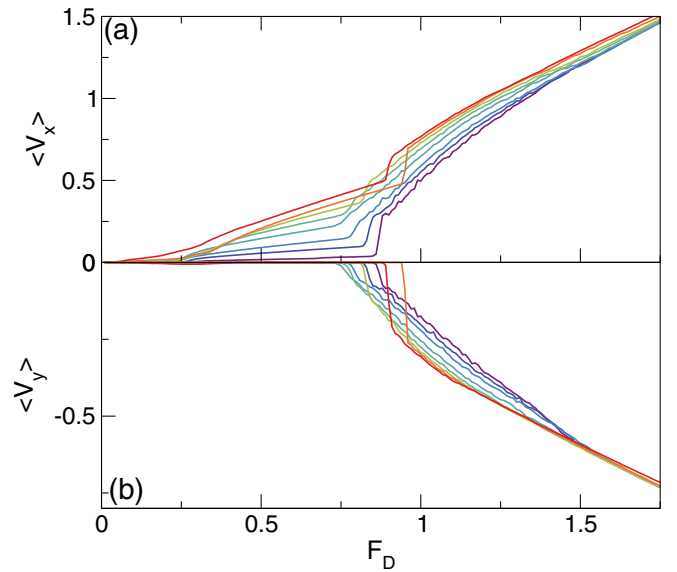


FIG. 27. (a) $\langle V_x \rangle$ and (b) $\langle V_y \rangle$ vs F_D for a sample with a square pinning array, $F_p = 1.5$, $\alpha_m/\alpha_d = 0.57$, and $\theta_{\text{sk}}^{\text{int}} = -30^\circ$ in which the driving force is applied to *all* of the skyrmions at $f = 1.01, 1.1392, 1.2416, 1.4512, 1.6576, 1.8656, 2.0$, and 2.29 , from bottom to top. There is regime in which the interstitial skyrmions move while the skyrmions trapped at pinning sites remain immobile. The upward jumps in the magnitude of $\langle V_x \rangle$ and $\langle V_y \rangle$ at higher drives correspond to the points at which the skyrmions at the pinning sites depin.

VIII. BULK DRIVING

In our system, we apply the driving force to only a single skyrmion. In experiment, this could be achieved by driving the skyrmion with a local tip; however, another possible approach is to apply a driving force to all of the skyrmions in the strong pinning regime where only the interstitial skyrmions move while the pinned skyrmions remain trapped. The skyrmions at the pinning sites have a well defined depinning threshold F_p , but skyrmions in the interstitial regions are pinned only via interactions with the skyrmions at the pinning sites, so they have a much lower depinning threshold F_c^{in} . These mobile interstitial skyrmions would have behavior very similar to that of the individually driven skyrmions we study. To demonstrate this, in Figs. 27(a) and 27(b), we plot $\langle V_x \rangle$ and $\langle V_y \rangle$, respectively, versus F_D for a sample with a square pinning array, $\alpha_m/\alpha_d = 0.5$ and $\theta_{\text{sk}} = -30^\circ$ where the driving force is applied to *all* of the skyrmions for fillings of $f = 1.01, 1.1392, 1.2416, 1.4512, 1.6576, 1.8656, 2.0$, and 2.29 . Here we work in the strong pinning regime with $F_p = 1.5$, providing a wide region of drive over which $\langle V_x \rangle$ is finite while $\langle V_y \rangle$ remains zero. In this regime, only the interstitial skyrmions are moving, but at higher drives when $\langle V_y \rangle$ becomes finite, the skyrmions in the pinning sites depin and the system enters a disordered flow state where skyrmions are able to move transverse to the pinning channels. The extent of the window of strictly interstitial motion diminishes as the filling increases, so the range $f = 1.0$ to 2.1 is where bulk driving can best mimic the effect of driving a single skyrmion. The interstitial motion window is bounded by the interstitial depinning threshold, which is controlled by the skyrmion density, and the

bulk depinning threshold, which is controlled by the pinning strength. Thus the window can be widened by using a strong pinning force and/or lower skyrmion densities.

IX. DISCUSSION

We expect that our results should be robust for any pinning geometries where commensuration effects occur. At matching fillings where the background skyrmions are ordered, the skyrmion Hall angle will be reduced and there can be a velocity boost effect when the intrinsic skyrmion Hall angle is greater than 45° . Other possible pinning array geometries include rectangular [130,131], 1D periodic [132], or even quasiperiodic [133,134]. As partially explored above, we also expect that thermal effects could enhance some of the phenomena we observe. Our results should be general to other systems coupled to periodic substrates where gyroscopic effects come into play.

In this work, we examined a wide range of intrinsic skyrmion Hall angles ranging from $\theta_{\text{sk}}^{\text{int}} = 5.75^\circ$ to $\theta_{\text{sk}}^{\text{int}} = 84^\circ$. For the square pinning array, we find that the velocity peaks for commensurate fillings are the most pronounced for $\theta_{\text{sk}}^{\text{int}} < 45^\circ$, while for larger skyrmion Hall angles, the velocity versus filling curves are smoother. Experimentally measured values for the skyrmion Hall angle range from a few degrees to as large as 22° [135,136] or 35° [50]; however there are several studies in which quite large skyrmion Hall angles of 45° [137,138] and even 55° [46] have been reported. These values are well within the range in which we find peaks in the skyrmion velocity and a reduction of the measured skyrmion Hall angle at commensurate fillings. The velocity boost where the skyrmion moves even faster than the drive does not occur until $\theta_{\text{sk}} > 45^\circ$, so such an effect could be possible in materials that have yet to be discovered. It is also possible that there are already existing systems containing small skyrmions in which higher Hall angles are present but have not yet been measured through imaging or transport.

In previous work by Reichhardt *et al.* [49], a single isolated skyrmion moving over a periodic substrate was studied. Those results correspond only to the 1 : 1 matching limit considered in the present work, but here we have investigated a wide range of fillings extending from $f = 0.01$ up to 4.0. Even at 1 : 1 matching, there can be differences between driving a single isolated skyrmion through fixed obstacles and driving an interstitial skyrmion through a pinned lattice of skyrmions, since the skyrmions within the pinning sites can shift positions slightly and develop distortions in their lattice that can affect the moving skyrmion. At other fillings, such collective effects or additional drag effects become even more important, as does the disordering of the background skyrmions and the frustration effects that appear for incommensurate fillings.

In our study, we are assuming a particle-based model, where distortions of the skyrmions themselves are neglected. A future direction would be to examine this same system with a continuum model that can capture the distortions of the driven skyrmion during collisions or near approaches with pinned background skyrmions. The particle-based model best represents lower densities of relatively small skyrmions interacting with a periodic nanostructured array of pinning sites.

X. SUMMARY

We have numerically examined the dynamics of individual skyrmions driven through an assembly of other skyrmions in the presence of a two-dimensional periodic pinning array. The Magnus force causes the driven skyrmion to move with a finite skyrmion Hall angle. Under a constant driving force, we find a nonmonotonic dependence of the skyrmion Hall angle on the density of the background skyrmions. In general, the skyrmion Hall angle drops to zero or is reduced in magnitude at commensurate conditions when the number of skyrmions is equal to an integer multiple of the number of pinning sites. There is also a peak in the net skyrmion velocity at the commensurate filling. At incommensurate fillings, the skyrmion Hall angle becomes finite again, but there is generally a decrease in the skyrmion Hall angle with increasing filling fraction. At commensurate fillings we find a two step depinning process and the motion of the driven skyrmion is well ordered, while at incommensurate fillings there is a single step depinning transition with disordered motion. For larger Magnus forces, additional locking effects can appear in which the motion of the driven skyrmion locks to different symmetry directions of the pinning lattice. In some cases, we find that increasing the Magnus force can enhance the effectiveness of the pinning, which is opposite to the behavior observed in a system with random pinning. This occurs because the Magnus force reduces the amount of channeling along the x direction. We show that our results are robust for both square and triangular pinning arrays. We also map out dynamical phase diagrams as a function of varied pinning strength, Magnus force contribution, and filling fraction.

ACKNOWLEDGMENTS

We gratefully acknowledge the support of the U.S. Department of Energy through the LANL/LDRD program for this work. This work was supported by the US Department of Energy through the Los Alamos National Laboratory. Los Alamos National Laboratory is operated by Triad National Security, LLC, for the National Nuclear Security Administration of the U.S. Department of Energy (Contract No. 892333218NCA000001).

-
- [1] S. Mühlbauer, B. Binz, F. Jonietz, C. Pfleiderer, A. Rosch, A. Neubauer, R. Georgii, and P. Böni, Skyrmion lattice in a chiral magnet, *Science* **323**, 915 (2009).
- [2] X. Z. Yu, Y. Onose, N. Kanazawa, J. H. Park, J. H. Han, Y. Matsui, N. Nagaosa, and Y. Tokura, Real-space observation

of a two-dimensional skyrmion crystal, *Nature (London)* **465**, 901 (2010).

- [3] N. Nagaosa and Y. Tokura, Topological properties and dynamics of magnetic skyrmions, *Nat. Nanotechnol.* **8**, 899 (2013).

- [4] A. Fert, N. Reyren, and V. Cros, Magnetic skyrmions: advances in physics and potential applications, *Nat. Rev. Mater.* **2**, 17031 (2017).
- [5] W. Jiang, G. Chen, K. Liu, J. Zang, S. G. E. te Velthuis, and A. Hoffmann, Skyrmions in magnetic multilayers, *Phys. Rep.* **704**, 1 (2017).
- [6] K. Everschor-Sitte, J. Masell, R. M. Reeve, and M. Kläui, Perspective: Magnetic skyrmions - Overview of recent progress in an active research field, *J. Appl. Phys.* **124**, 240901 (2018).
- [7] M. T. Birch, D. Cortés-Ortuño, L. A. Turnbull, M. N. Wilson, F. Gross, N. Traeger, A. Laurensen, N. Bukin, S. H. Moody, M. Weigand, G. Schuetz, H. Popescu, R. Fan, P. Steadman, J. A. T. Verezhak, G. Balakrishnan, J. C. Loudon, A. C. Twitchett-Harrison, O. Hovorka, H. Fangohr *et al.*, Real-space imaging of confined magnetic skyrmion tubes, *Nat. Commun.* **11**, 1726 (2020).
- [8] A. N. Bogdanov and C. Panagopoulos, Physical foundations and basic properties of magnetic skyrmions, *Nat. Rev. Phys.* **2**, 492 (2020).
- [9] W. Jiang, P. Upadhyaya, W. Zhang, G. Yu, M. B. Jungfleisch, F. Y. Fradin, J. E. Pearson, Y. Tserkovnyak, K. L. Wang, O. Heinonen, S. G. E. te Velthuis, and A. Hoffmann, Blowing magnetic skyrmion bubbles, *Science* **349**, 283 (2015).
- [10] C. Moreau-Luchaire, C. Moutafis, N. Reyren, J. Sampaio, C. A. F. Vaz, N. Van Horne, K. Bouzehouane, K. Garcia, C. Deranlot, P. Warnicke, P. Wohlhüter, J. M. George, M. Weigand, J. Raabe, V. Cros, and A. Fert, Additive interfacial chiral interaction in multilayers for stabilization of small individual skyrmions at room temperature, *Nat. Nanotechnol.* **11**, 444 (2016).
- [11] O. Boulle, J. Vogel, H. Yang, S. Pizzini, D. de Souza Chaves, A. Locatelli, T. O. Menteş, A. Sala, L. D. Buda-Prejbeanu, O. Klein, M. Belmeguenai, Y. Roussigné, A. Stashkevich, S. M. Chérif, L. Aballe, M. Foerster, M. Chshiev, S. Auffret, I. M. Miron, and G. Gaudin, Room-temperature chiral magnetic skyrmions in ultrathin magnetic nanostructures, *Nat. Nanotechnol.* **11**, 449 (2016).
- [12] A. Soumyanarayanan, M. Raju, A. L. G. Oyarce, A. K. C. Tan, M.-Y. Im, A. P. Petrović, P. Ho, K. H. Khoo, M. Tran, C. K. Gan, F. Ernult, and C. Panagopoulos, Tunable room-temperature magnetic skyrmions in Ir/Fe/Co/Pt multilayers, *Nat. Mater.* **16**, 898 (2017).
- [13] F. Jonietz, S. Mühlbauer, C. Pfleiderer, A. Neubauer, W. Münzer, A. Bauer, T. Adams, R. Georgii, P. Böni, R. A. Duine, K. Everschor, M. Garst, and A. Rosch, Spin transfer torques in MnSi at ultralow current densities, *Science* **330**, 1648 (2010).
- [14] J. Zang, M. Mostovoy, J. H. Han, and N. Nagaosa, Dynamics of Skyrmion Crystals in Metallic Thin Films, *Phys. Rev. Lett.* **107**, 136804 (2011).
- [15] X. Z. Yu, N. Kanazawa, W. Z. Zhang, T. Nagai, T. Hara, K. Kimoto, Y. Matsui, Y. Onose, and Y. Tokura, Skyrmion flow near room temperature in an ultralow current density, *Nat. Commun.* **3**, 988 (2012).
- [16] S.-Z. Lin, C. Reichhardt, C. D. Batista, and A. Saxena, Driven Skyrmions and Dynamical Transitions in Chiral Magnets, *Phys. Rev. Lett.* **110**, 207202 (2013).
- [17] D. Liang, J. P. DeGrave, M. J. Stolt, Y. Tokura, and S. Jin, Current-driven dynamics of skyrmions stabilized in MnSi nanowires revealed by topological Hall effect, *Nat. Commun.* **6**, 8217 (2015).
- [18] S. Woo, K. Litzius, B. Krüger, M.-Y. Im, L. Caretta, K. Richter, M. Mann, A. Krone, R. M. Reeve, M. Weigand, P. Agrawal, I. Lemesh, M.-A. Mawass, P. Fischer, M. Kläui, and G. S. D. Beach, Observation of room-temperature magnetic skyrmions and their current-driven dynamics in ultrathin metallic ferromagnets, *Nat. Mater.* **15**, 501 (2016).
- [19] W. Legrand, D. Maccariello, N. Reyren, K. Garcia, C. Moutafis, C. Moreau-Luchaire, S. Coffin, K. Bouzehouane, V. Cros, and A. Fert, Room-temperature current-induced generation and motion of sub-100 nm skyrmions, *Nano Lett.* **17**, 2703 (2017).
- [20] S. A. Montoya, R. Tolley, I. Gilbert, S.-G. Je, M.-Y. Im, and E. E. Fullerton, Spin-orbit torque induced dipole skyrmion motion at room temperature, *Phys. Rev. B* **98**, 104432 (2018).
- [21] A. Fert, V. Cros, and J. Sampaio, Skyrmions on the track, *Nat. Nanotechnol.* **8**, 152 (2013).
- [22] R. Tomasello, E. Martinez, R. Zivieri, L. Torres, M. Carpentieri, and G. Finocchio, A strategy for the design of skyrmion racetrack memories, *Sci. Rep.* **4**, 6784 (2014).
- [23] D. Pinna, G. Bourianoff, and K. Everschor-Sitte, Reservoir Computing with Random Skyrmion Textures, *Phys. Rev. Applied* **14**, 054020 (2020).
- [24] K. M. Song, J.-S. Jeong, B. Pan, X. Zhang, J. Xia, S. Cha, T.-E. Park, K. Kim, S. Finizio, J. Raabe, J. Chang, J. Zhou, W. Zhao, W. Kang, H. Ju, and S. Woo, Skyrmion-based artificial synapses for neuromorphic computing, *Nat. Electron.* **3**, 148 (2020).
- [25] C. Reichhardt, C. J. O. Reichhardt, and M. V. Milošević, Statics and dynamics of skyrmions interacting with pinning: a review, [arXiv:2102.10464](https://arxiv.org/abs/2102.10464) [Rev. Mod. Phys. (to be published)].
- [26] Y.-H. Liu and Y.-Q. Li, A mechanism to pin skyrmions in chiral magnets, *J. Phys.: Condens. Matter* **25**, 076005 (2013).
- [27] J. Iwasaki, M. Mochizuki, and N. Nagaosa, Universal current-velocity relation of skyrmion motion in chiral magnets, *Nat. Commun.* **4**, 1463 (2013).
- [28] A. Salimath, A. About, A. Brataas, and A. Manchon, Current-driven skyrmion depinning in magnetic granular films, *Phys. Rev. B* **99**, 104416 (2019).
- [29] L. Xiong, B. Zheng, M. H. Jin, and N. J. Zhou, Collective transport properties of skyrmions on the depinning phase transition, *Phys. Rev. B* **100**, 064426 (2019).
- [30] R. Juge, S.-G. Je, D. de SouzaChaves, L. D. Buda-Prejbeanu, J. Pena Garcia, J. Nath, I. M. Miron, K. G. Rana, L. Aballe, M. Foerster, F. Genuzio, T. O. Menteş, A. Locatelli, F. Maccherozzi, S. S. Dhesi, M. Belmeguenai, Y. Roussigné, S. Auffret, S. Pizzini, G. Gaudin *et al.*, Current-Driven Skyrmion Dynamics and Drive-Dependent Skyrmion Hall Effect in an Ultrathin Film, *Phys. Rev. Applied* **12**, 044007 (2019).
- [31] N. Del-Valle, J. Castell-Queralt, L. González-Gómez, and C. Navau, Defect modeling in skyrmionic ferromagnetic systems, *APL Mater.* **10**, 010702 (2022).
- [32] D. Stosic, T. B. Ludermir, and M. V. Milošević, Pinning of magnetic skyrmions in a monolayer Co film on Pt(111): Theoretical characterization and exemplified utilization, *Phys. Rev. B* **96**, 214403 (2017).
- [33] I. L. Fernandes, J. Bouaziz, S. Blügel, and S. Lounis, Universality of defect-skyrmion interaction profiles, *Nat. Commun.* **9**, 4395 (2018).

- [34] C. Navau, N. Del-Valle, and A. Sanchez, Interaction of isolated skyrmions with point and linear defects, *J. Magn. Magn. Mater.* **465**, 709 (2018).
- [35] W. Koshibae and N. Nagaosa, Theory of current-driven skyrmions in disordered magnets, *Sci. Rep.* **8**, 6328 (2018).
- [36] S.-Z. Lin, C. Reichhardt, C. D. Batista, and A. Saxena, Particle model for skyrmions in metallic chiral magnets: Dynamics, pinning, and creep, *Phys. Rev. B* **87**, 214419 (2013).
- [37] C. Reichhardt and C. J. O. Reichhardt, Thermal creep and the skyrmion Hall angle in driven skyrmion crystals, *J. Phys.: Condens. Matter* **31**, 07LT01 (2018).
- [38] K. Litzius, J. Leliaert, P. Bassirian, D. Rodrigues, S. Kromin, I. Lemes, J. Zázvorka, K.-J. Lee, J. Mulkers, N. Kerber, D. Heinze, N. Keil, R. M. Reeve, M. Weigand, B. Van Waeyenberge, G. Schütz, K. Everschor-Sitte, G. S. D. Beach, and M. Kläui, The role of temperature and drive current in skyrmion dynamics, *Nat. Electron.* **3**, 30 (2020).
- [39] B. Göbel, I. Mertig, and O. A. Tretiakov, Beyond skyrmions: Review and perspectives of alternative magnetic quasiparticles, *Phys. Rep.* **895**, 1 (2021).
- [40] J. Barker and O. A. Tretiakov, Static and Dynamical Properties of Antiferromagnetic Skyrmions in the Presence of Applied Current and Temperature, *Phys. Rev. Lett.* **116**, 147203 (2016).
- [41] W. Legrand, D. Maccariello, F. Ajejas, S. Collin, A. Vecchiola, K. Bouzehouane, N. Reyren, V. Cros, and A. Fert, Room-temperature stabilization of antiferromagnetic skyrmions in synthetic antiferromagnets, *Nat. Mater.* **19**, 34 (2020).
- [42] A. K. Nayak, V. Kumar, T. Ma, P. Werner, E. Pippel, R. Sahoo, F. Damay, U. K. Roessler, C. Felser, and S. S. P. Parkin, Magnetic antiskyrmions above room temperature in tetragonal Heusler materials, *Nature (London)* **548**, 561 (2017).
- [43] A. A. Kovalev and S. Sandhoefner, Skyrmions and anti-skyrmions in quasi-two-dimensional magnets, *Front. Phys.* **6**, 98 (2018).
- [44] X. Z. Yu, W. Koshibae, Y. Tokunaga, K. Shibata, Y. Taguchi, N. Nagaosa, and Y. Tokura, Transformation between meron and skyrmion topological spin textures in a chiral magnet, *Nature (London)* **564**, 95 (2018).
- [45] K. Everschor-Sitte and M. Sitte, Real-space Berry phases: Skyrmion soccer (invited), *J. Appl. Phys.* **115**, 172602 (2014).
- [46] R. Brearton, L. A. Turnbull, J. A. T. Verezhak, G. Balakrishnan, P. D. Hatton, G. van der Laan, and T. Hesjedal, Deriving the skyrmion Hall angle from skyrmion lattice dynamics, *Nat. Commun.* **12**, 2723 (2021).
- [47] J. Müller and A. Rosch, Capturing of a magnetic skyrmion with a hole, *Phys. Rev. B* **91**, 054410 (2015).
- [48] C. Reichhardt, D. Ray, and C. J. Olson Reichhardt, Quantized transport for a skyrmion moving on a two-dimensional periodic substrate, *Phys. Rev. B* **91**, 104426 (2015).
- [49] C. Reichhardt, D. Ray, and C. J. Olson Reichhardt, Collective Transport Properties of Driven Skyrmions with Random Disorder, *Phys. Rev. Lett.* **114**, 217202 (2015).
- [50] W. Jiang, X. Zhang, G. Yu, W. Zhang, X. Wang, M. B. Jungfleisch, J. E. Pearson, X. Cheng, O. Heinonen, K. L. Wang, Y. Zhou, A. Hoffmann, and S. G. E. te Velthuis, Direct observation of the skyrmion Hall effect, *Nat. Phys.* **13**, 162 (2017).
- [51] J.-V. Kim and M.-W. Yoo, Current-driven skyrmion dynamics in disordered films, *Appl. Phys. Lett.* **110**, 132404 (2017).
- [52] S. A. Díaz, C. J. O. Reichhardt, D. P. Arovas, A. Saxena, and C. Reichhardt, Fluctuations and noise signatures of driven magnetic skyrmions, *Phys. Rev. B* **96**, 085106 (2017).
- [53] I. L. Fernandes, J. Chico, and S. Lounis, Impurity-dependent gyrotropic motion, deflection and pinning of current-driven ultrasmall skyrmions in PdFe/Ir(111) surface, *J. Phys.: Condens. Matter* **32**, 425802 (2020).
- [54] X. Z. Yu, D. Morikawa, K. Nakajima, K. Shibata, N. Kanazawa, T. Arima, N. Nagaosa, and Y. Tokura, Motion tracking of 80-nm-size skyrmions upon directional current injections, *Sci. Adv.* **6**, eaaz9744 (2020).
- [55] L. Peng, K. Karube, Y. Taguchi, N. Nagaosa, Y. Tokura, and X. Yu, Dynamic transition of current-driven single-skyrmion motion in a room-temperature chiral-lattice magnet, *Nat. Commun.* **12**, 6797 (2021).
- [56] K. Litzius, I. Lemes, B. Krüger, P. Bassirian, L. Caretta, K. Richter, F. Büttner, K. Sato, O. A. Tretiakov, J. Förster, R. M. Reeve, M. Weigand, L. Bykova, H. Stoll, G. Schütz, G. S. D. Beach, and M. Kläui, Skyrmion Hall effect revealed by direct time-resolved X-ray microscopy, *Nat. Phys.* **13**, 170 (2017).
- [57] K. Zeissler, S. Finizio, C. Barton, A. J. Huxtable, J. Massey, J. Raabe, A. V. Sadovnikov, S. A. Nikitov, R. Brearton, T. Hesjedal, G. van der Laan, M. C. Rosamond, E. H. Linfield, G. Burnell, and C. H. Marrows, Diameter-independent skyrmion Hall angle observed in chiral magnetic multilayers, *Nat. Commun.* **11**, 428 (2020).
- [58] I. L. Fernandes, M. Bouhassoune, and S. Lounis, Defect-implantation for the all-electrical detection of non-collinear spin-textures, *Nat. Commun.* **11**, 1602 (2020).
- [59] K. Migita, K. Yamada, and Y. Nakatani, Controlling skyrmion motion in an angelfish-type racetrack memory by an AC magnetic field, *Appl. Phys. Express* **13**, 073003 (2020).
- [60] B. Göbel and I. Mertig, Skyrmion ratchet propagation: Utilizing the skyrmion Hall effect in AC racetrack storage devices, *Sci. Rep.* **11**, 3020 (2021).
- [61] R. Juge, K. Bairagi, K. G. Rana, J. Vogel, M. Sall, D. Maily, V. T. Pham, Q. Zhang, N. Sisodia, M. Foerster, L. Aballe, M. Belmuguenai, Y. Roussigné, S. Auffret, L. D. Buda-Prejbeanu, G. Gaudin, D. Ravelosona, and O. Boulle, Helium ions put magnetic skyrmions on the track, *Nano Lett.* **21**, 2989 (2021).
- [62] P. Bak, Commensurate phases, incommensurate phases and the devil's staircase, *Rep. Prog. Phys.* **45**, 587 (1982).
- [63] A. Vanossi, N. Manini, M. Urbakh, S. Zapperi, and E. Tosatti, Colloquium: Modeling friction: From nanoscale to mesoscale, *Rev. Mod. Phys.* **85**, 529 (2013).
- [64] C. Reichhardt and C. J. Olson, Novel Colloidal Crystalline States on Two-Dimensional Periodic Substrates, *Phys. Rev. Lett.* **88**, 248301 (2002).
- [65] K. Mangold, P. Leiderer, and C. Bechinger, Phase Transitions of Colloidal Monolayers in Periodic Pinning Arrays, *Phys. Rev. Lett.* **90**, 158302 (2003).
- [66] Y. Huang, W. Li, C. Reichhardt, C. J. O. Reichhardt, and Y. Feng, Phonon spectra of a two-dimensional solid dusty plasma modified by two-dimensional periodic substrates, *Phys. Rev. E* **105**, 015202 (2022).
- [67] Y. Xu, S. Liu, D. A. Rhodes, K. Watanabe, T. Taniguchi, J. Hone, V. Elser, K. F. Mak, and J. Shan, Correlated insulating states at fractional fillings of moiré superlattices, *Nature (London)* **587**, 214 (2020).

- [68] S. Tung, V. Schweikhard, and E. A. Cornell, Observation of Vortex Pinning in Bose-Einstein Condensates, *Phys. Rev. Lett.* **97**, 240402 (2006).
- [69] M. Lewenstein, A. Sanpera, V. Ahufinger, B. Damski, A. Sen(De), and U. Sen, Ultracold atomic gases in optical lattices: mimicking condensed matter physics and beyond, *Adv. Phys.* **56**, 243 (2007).
- [70] M. Baert, V. V. Metlushko, R. Jonckheere, V. V. Moshchalkov, and Y. Bruynseraede, Composite Flux-Line Lattices Stabilized in Superconducting Films by a Regular Array of Artificial Defects, *Phys. Rev. Lett.* **74**, 3269 (1995).
- [71] K. Harada, O. Kamimura, H. Kasai, T. Matsuda, A. Tonomura, and V. V. Moshchalkov, Direct observation of vortex dynamics in superconducting films with regular arrays of defects, *Science* **274**, 1167 (1996).
- [72] J. I. Martín, M. Vélez, J. Nogués, and I. K. Schuller, Flux Pinning in a Superconductor by an Array of Submicrometer Magnetic Dots, *Phys. Rev. Lett.* **79**, 1929 (1997).
- [73] C. Reichhardt, C. J. Olson, and F. Nori, Commensurate and incommensurate vortex states in superconductors with periodic pinning arrays, *Phys. Rev. B* **57**, 7937 (1998).
- [74] G. R. Berdiyrov, M. V. Milošević, and F. M. Peeters, Novel Commensurability Effects in Superconducting Films with Antidot Arrays, *Phys. Rev. Lett.* **96**, 207001 (2006).
- [75] I. A. Sadovskyy, Y. L. Wang, Z.-L. Xiao, W.-K. Kwok, and A. Glatz, Effect of hexagonal patterned arrays and defect geometry on the critical current of superconducting films, *Phys. Rev. B* **95**, 075303 (2017).
- [76] J. Gutierrez, A. V. Silhanek, J. Van de Vondel, W. Gillijns, and V. V. Moshchalkov, Transition from turbulent to nearly laminar vortex flow in superconductors with periodic pinning, *Phys. Rev. B* **80**, 140514 (2009).
- [77] A. Vanossi, N. Manini, and E. Tosatti, Static and dynamic friction in sliding colloidal monolayers, *Proc. Natl. Acad. Sci. USA* **109**, 16429 (2012).
- [78] T. Bohlein, J. Mikhael, and C. Bechinger, Observation of kinks and antikinks in colloidal monolayers driven across ordered surfaces, *Nat. Mater.* **11**, 126 (2012).
- [79] C. Reichhardt and F. Nori, Phase Locking, Devil's Staircases, Farey Trees, and Arnold Tongues in Driven Vortex Lattices with Periodic Pinning, *Phys. Rev. Lett.* **82**, 414 (1999).
- [80] P. T. Korda, M. B. Taylor, and D. G. Grier, Kinetically Locked-In Colloidal Transport in an Array of Optical Tweezers, *Phys. Rev. Lett.* **89**, 128301 (2002).
- [81] A. V. Silhanek, L. Van Look, S. Raedts, R. Jonckheere, and V. V. Moshchalkov, Guided vortex motion in superconductors with a square antidot array, *Phys. Rev. B* **68**, 214504 (2003).
- [82] A. Gopinathan and D. G. Grier, Statistically Locked-In Transport through Periodic Potential Landscapes, *Phys. Rev. Lett.* **92**, 130602 (2004).
- [83] X. Cao, E. Panizon, A. Vanossi, N. Manini, and C. Bechinger, Orientational and directional locking of colloidal clusters driven across periodic surfaces, *Nat. Phys.* **15**, 776 (2019).
- [84] R. L. Stoop, A. V. Straube, T. H. Johansen, and P. Tierno, Collective Directional Locking of Colloidal Monolayers on a Periodic Substrate, *Phys. Rev. Lett.* **124**, 058002 (2020).
- [85] N. P. Vizarim, C. Reichhardt, C. J. O. Reichhardt, and P. A. Venegas, Skyrmion dynamics and topological sorting on periodic obstacle arrays, *New J. Phys.* **22**, 053025 (2020).
- [86] J. Feilhauer, S. Saha, J. Tobik, M. Zelent, L. J. Heyderman, and M. Mruczkiewicz, Controlled motion of skyrmions in a magnetic antidot lattice, *Phys. Rev. B* **102**, 184425 (2020).
- [87] F. Ma, C. Reichhardt, W. Gan, C. J. Olson Reichhardt, and W. S. Lew, Emergent geometric frustration of artificial magnetic skyrmion crystals, *Phys. Rev. B* **94**, 144405 (2016).
- [88] C. Reichhardt, D. Ray, and C. J. O. Reichhardt, Nonequilibrium phases and segregation for skyrmions on periodic pinning arrays, *Phys. Rev. B* **98**, 134418 (2018).
- [89] X. Zhang, J. Xia, K. Shirai, H. Fujiwara, O. A. Tretiakov, M. Ezawa, Y. Zhou, and X. Liu, Configurable pixelated skyrmions on nanoscale magnetic grids, *Commun. Phys.* **4**, 255 (2021).
- [90] S. Saha, M. Zelent, S. Finizio, M. Mruczkiewicz, S. Tacchi, A. K. Suszka, S. Wintz, N. S. Bingham, J. Raabe, M. Krawczyk, and L. J. Heyderman, Formation of Néel-type skyrmions in an antidot lattice with perpendicular magnetic anisotropy, *Phys. Rev. B* **100**, 144435 (2019).
- [91] X. Ma, C. J. O. Reichhardt, and C. Reichhardt, Manipulation of individual superconducting vortices and stick-slip motion in periodic pinning arrays, *Phys. Rev. B* **97**, 214521 (2018).
- [92] C. J. O. Reichhardt and C. Reichhardt, Active rheology and anti-commensuration effects for driven probe particles on two dimensional periodic pinning substrates, *Phys. Rev. Research* **4**, 013190 (2022).
- [93] C. Reichhardt and C. J. O. Reichhardt, Dynamics and non-monotonic drag for individually driven skyrmions, *Phys. Rev. B* **104**, 064441 (2021).
- [94] C. J. O. Reichhardt and C. Reichhardt, Fluctuations and pinning for individually manipulated skyrmions, *Front. Phys.* **9**, 767491 (2021).
- [95] E. W. J. Straver, J. E. Hoffman, O. M. Auslaender, D. Rugar, and K. A. Moler, Controlled manipulation of individual vortices in a superconductor, *Appl. Phys. Lett.* **93**, 172514 (2008).
- [96] O. M. Auslaender, L. Luan, E. W. J. Straver, J. E. Hoffman, N. C. Koshnick, E. Zeldov, D. A. Bonn, R. Liang, W. N. Hardy, and K. A. Moler, Mechanics of individual isolated vortices in a cuprate superconductor, *Nat. Phys.* **5**, 35 (2009).
- [97] I. S. Veshchunov, W. Magrini, S. V. Mironov, A. G. Godin, J. B. Trebbia, A. I. Buzdin, Ph. Tamarat, and B. Lounis, Optical manipulation of single flux quanta, *Nat. Commun.* **7**, 12801 (2016).
- [98] A. Kremen, S. Wissberg, N. Haham, E. Persky, Y. Frenkel, and B. Kalisky, Mechanical control of individual superconducting vortices, *Nano Lett.* **16**, 1626 (2016).
- [99] C. Hanneken, A. Kubetzka, K. von Bergmann, and R. Wiesendanger, Pinning and movement of individual nanoscale magnetic skyrmions via defects, *New J. Phys.* **18**, 055009 (2016).
- [100] C. Wang, D. Xiao, X. Chen, Y. Zhou, and Y. Liu, Manipulating and trapping skyrmions by magnetic field gradients, *New J. Phys.* **19**, 083008 (2017).
- [101] A. Casiraghi, H. Corte-León, M. Vafaee, F. Garcia-Sanchez, G. Durin, M. Pasquale, G. Jakob, M. Kläui, and O. Kazakova, Individual skyrmion manipulation by local magnetic field gradients, *Commun. Phys.* **2**, 145 (2019).
- [102] W. Yang, H. Yang, Y. Cao, and P. Yan, Photonic orbital angular momentum transfer and magnetic skyrmion rotation, *Opt. Express* **26**, 8778 (2018).
- [103] X.-G. Wang, L. Chotorlishvili, V. K. Dugaev, A. Ernst, I. V. Maznichenko, N. Arnold, C. Jia, J. Berakdar, I. Mertig, and J.

- Barnas, The optical tweezer of skyrmions, *npj Comput. Mater.* **6**, 140 (2020).
- [104] T. Hirose, J. Klinovaja, D. Loss, and S. A. Díaz, Laser-Controlled Real- and Reciprocal-Space Topology in Multiferroic Insulators, *Phys. Rev. Lett.* **128**, 037201 (2022).
- [105] P. Habdas, D. Schaar, A. C. Levitt, and E. R. Weeks, Forced motion of a probe particle near the colloidal glass transition, *Europhys. Lett.* **67**, 477 (2004).
- [106] T. M. Squires and J. F. Brady, A simple paradigm for active and nonlinear microrheology, *Phys. Fluids* **17**, 073101(2005).
- [107] R. P. A. Dullens and C. Bechinger, Shear Thinning and Local Melting of Colloidal Crystals, *Phys. Rev. Lett.* **107**, 138301 (2011).
- [108] I. Gazuz, A. M. Puertas, Th. Voigtmann, and M. Fuchs, Active and Nonlinear Microrheology in Dense Colloidal Suspensions, *Phys. Rev. Lett.* **102**, 248302 (2009).
- [109] R. N. Zia, Active and passive microrheology: Theory and simulation, *Annu. Rev. Fluid Mech.* **50**, 371 (2018).
- [110] J. A. Drocco, M. B. Hastings, C. J. Olson Reichhardt, and C. Reichhardt, Multiscaling at point J : Jamming is a critical phenomenon, *Phys. Rev. Lett.* **95**, 088001 (2005).
- [111] R. Candelier and O. Dauchot, Journey of an intruder through the fluidization and jamming transitions of a dense granular media, *Phys. Rev. E* **81**, 011304 (2010).
- [112] E. Kolb, P. Cixous, N. Gaudouen, and T. Darnige, Rigid intruder inside a two-dimensional dense granular flow: Drag force and cavity formation, *Phys. Rev. E* **87**, 032207 (2013).
- [113] C. Reichhardt and C. J. Olson Reichhardt, Active microrheology in active matter systems: Mobility, intermittency, and avalanches, *Phys. Rev. E* **91**, 032313 (2015).
- [114] C. J. Olson Reichhardt and C. Reichhardt, Viscous decoupling transitions for individually dragged particles in systems with quenched disorder, *Phys. Rev. E* **78**, 011402 (2008).
- [115] C. Reichhardt, Vortices wiggled and dragged, *Nat. Phys.* **5**, 15 (2009).
- [116] C. J. O. Reichhardt and C. Reichhardt, Active rheology in odd viscosity systems, *Europhys. Lett.* **137**, 66004 (2022).
- [117] D. Banerjee, A. Souslov, A. G. Abanov, and V. Vitelli, Odd viscosity in chiral active fluids, *Nat. Commun.* **8**, 1573 (2017).
- [118] V. Soni, E. S. Bililign, S. Magkiriadou, S. Sacanna, D. Bartolo, M. J. Shelley, and W. T. M. Irvine, The odd free surface flows of a colloidal chiral fluid, *Nat. Phys.* **15**, 1188 (2019).
- [119] C. Reichhardt and C. J. O. Reichhardt, Active microrheology, Hall effect, and jamming in chiral fluids, *Phys. Rev. E* **100**, 012604 (2019).
- [120] J. Iwasaki, W. Koshibae, and N. Nagaosa, Colossal spin transfer torque effect on skyrmion along the edge, *Nano Lett.* **14**, 4432 (2014).
- [121] J. Castell-Queralt, L. Gonzalez-Gomez, N. Del-Valle, A. Sanchez, and C. Navau, Accelerating, guiding, and compressing skyrmions by defect rails, *Nanoscale* **11**, 12589 (2019).
- [122] L.-M. Kern, B. Pfau, V. Deinhart, M. Schneider, C. Klose, K. Gerlinger, S. Wittrock, D. Engel, I. Will, C. M. Günther, R. Liefnerink, J. H. Mentink, S. Wintz, M. Weigand, M.-J. Huang, R. Battistelli, D. Metternich, F. Büttner, K. Höflich, and S. Eisebitt, Deterministic generation and guided motion of magnetic skyrmions by focused He⁺-ion irradiation, *Nano Lett.* **22**, 4028 (2022).
- [123] X. Gong, K. Y. Jing, J. Lu, and X. R. Wang, Skyrmion pinning by disk-shaped defects, *Phys. Rev. B* **105**, 094437 (2022).
- [124] A. N. Grigorenko, S. J. Bending, M. J. Van Bael, M. Lange, V. V. Moshchalkov, H. Fangohr, and P. A. J. de Groot, Symmetry Locking and Commensurate Vortex Domain Formation in Periodic Pinning Arrays, *Phys. Rev. Lett.* **90**, 237001 (2003).
- [125] C. Reichhardt and N. Grønbech-Jensen, Critical currents and vortex states at fractional matching fields in superconductors with periodic pinning, *Phys. Rev. B* **63**, 054510 (2001).
- [126] A. Duzgun, C. Nisoli, C. J. O. Reichhardt, and C. Reichhardt, Commensurate states and pattern switching via liquid crystal skyrmions trapped in a square lattice, *Soft Matter* **16**, 3338 (2020).
- [127] I. G. Arjana, I. L. Fernandes, J. Chico, and S. Lounis, Sub-nanoscale atom-by-atom crafting of skyrmion-defect interaction profiles, *Sci. Rep.* **10**, 14655 (2020).
- [128] C. J. Olson Reichhardt and C. Reichhardt, Fluctuations, jamming, and yielding for a driven probe particle in disordered disk assemblies, *Phys. Rev. E* **82**, 051306 (2010).
- [129] T. Sato, W. Koshibae, A. Kikkawa, T. Yokouchi, H. Oike, Y. Taguchi, N. Nagaosa, Y. Tokura, and F. Kagawa, Slow steady flow of a skyrmion lattice in a confined geometry probed by narrow-band resistance noise, *Phys. Rev. B* **100**, 094410 (2019).
- [130] C. Reichhardt, G. T. Zimányi, and N. Grønbech-Jensen, Complex dynamical flow phases and pinning in superconductors with rectangular pinning arrays, *Phys. Rev. B* **64**, 014501 (2001).
- [131] M. Velez, D. Jaque, J. I. Martín, M. I. Montero, I. K. Schuller, and J. L. Vicent, Vortex lattice channeling effects in Nb films induced by anisotropic arrays of mesoscopic pinning centers, *Phys. Rev. B* **65**, 104511 (2002).
- [132] Q. Le Thien, D. McDermott, C. J. Olson Reichhardt, and C. Reichhardt, Orientational ordering, buckling, and dynamic transitions for vortices interacting with a periodic quasi-one-dimensional substrate, *Phys. Rev. B* **93**, 014504 (2016).
- [133] M. Kemmler, C. Gürlich, A. Sterck, H. Pöhler, M. Neuhaus, M. Siegel, R. Kleiner, and D. Koelle, Commensurability Effects in Superconducting Nb Films with Quasiperiodic Pinning Arrays, *Phys. Rev. Lett.* **97**, 147003 (2006).
- [134] C. Reichhardt and C. J. Olson Reichhardt, Dynamical Ordering and Directional Locking for Particles Moving over Quasicrystalline Substrates, *Phys. Rev. Lett.* **106**, 060603 (2011).
- [135] A. K. C. Tan, P. Ho, J. Lourembam, L. Huang, H. K. Tan, C. J. O. Reichhardt, C. Reichhardt, and A. Soumyanarayanan, Visualizing the strongly reshaped skyrmion Hall effect in multilayer wire devices, *Nat. Commun.* **12**, 4252 (2021).
- [136] S. Yang, K.-W. Moon, C. Kim, D.-H. Kim, J. Shin, J. Hong, S. K. Kim, and C. Hwang, Control of the half-skyrmion Hall effect and its application to adder-subtractor, *Adv. Quantum Technol.* **4**, 2000060 (2021).
- [137] S. Zhang, X. Zhang, J. Zhang, A. Ganguly, J. Xia, Y. Wen, Q. Zhang, G. Yu, Z. Hou, W. Wang, Y. Peng, G. Xiao, A. Manchon, J. Kosel, Y. Zhou, and X.-X. Zhang, Direct imaging of an inhomogeneous electric current distribution using the trajectory of magnetic half-skyrmions, *Sci. Adv.* **6**, eaay1876 (2020).
- [138] V. Ahrens, L. Gnoli, D. Giuliano, S. Mendisch, M. Kiechle, F. Riente, and M. Becherer, Skyrmion velocities in FIB irradiated W/CoFeB/MgO thin films, *AIP Adv.* **12**, 035325 (2022).